

1 **The Education and Research 3D Radiative Transfer Toolbox (EaR<sup>3</sup>T) – Towards the**  
2 **Mitigation of 3D Bias in Airborne and Spaceborne Passive Imagery Cloud Retrievals**

3

4 Hong Chen<sup>1,2</sup>, K. Sebastian Schmidt<sup>1,2</sup>, Steven T. Massie<sup>2</sup>, Vikas Nataraja<sup>2</sup>, Matthew S. Norgren<sup>2</sup>,  
5 Jake J. Gristey<sup>3,4</sup>, Graham Feingold<sup>4</sup>, Robert E. Holz<sup>5</sup>, Hironobu Iwabuchi<sup>6</sup>

6

7

8 <sup>1</sup>Department of Atmospheric and Oceanic Sciences, University of Colorado, Boulder, CO, USA

9 <sup>2</sup>Laboratory for Atmospheric and Space Physics, University of Colorado, Boulder, CO, USA

10 <sup>3</sup>Cooperative Institute for Research in Environmental Sciences, University of Colorado,  
11 Boulder, CO, USA

12 <sup>4</sup>NOAA Chemical Sciences Laboratory, Boulder, CO, USA

13 <sup>5</sup>Space Science and Engineering Center, University of Wisconsin–Madison, Madison, WI, USA

14 <sup>6</sup>Center for Atmospheric and Oceanic Studies, Tohoku University, Sendai, Miyagi, Japan

15

16

17

18

19 *Correspondence to:* Hong Chen (hong.chen-1@colorado.edu)

20 **Abstract**

21 We introduce the Education and Research 3D Radiative Transfer Toolbox (EaR<sup>3</sup>T, [pronounced](#)  
22 [\[3:t\]](#)) for quantifying and mitigating artifacts in atmospheric radiation science algorithms due to spatially  
23 inhomogeneous clouds and surfaces, and show the benefits of automated, realistic radiance and irradiance  
24 generation along extended satellite orbits, flight tracks from entire aircraft field missions, and synthetic data  
25 generation from model data. EaR<sup>3</sup>T is a modularized Python package that provides high-level interfaces to  
26 automate the process of 3D radiative transfer (RT) calculations. After introducing the package, we present  
27 initial findings from four applications, which are intended as blueprints to future in-depth scientific studies.  
28 The first two applications use EaR<sup>3</sup>T as a satellite radiance simulator for the NASA Orbiting Carbon  
29 Observatory 2 (OCO-2) and Moderate Resolution Imaging Spectroradiometer (MODIS) missions, which  
30 generate synthetic satellite observations with 3D-RT on the basis of cloud field properties from  
31 imagery-based retrievals and other input data. In the case of inhomogeneous cloud fields, we show that the  
32 synthetic radiances are often inconsistent with the original radiance measurements. This lack of radiance  
33 consistency points to biases in heritage imagery cloud retrievals due to sub-pixel resolution clouds and  
34 3D-RT effects. They come to light because the simulator's 3D-RT engine replicates processes in nature that  
35 conventional 1D-RT retrievals do not capture. We argue that 3D radiance consistency (closure) can serve  
36 as a metric for assessing the performance of a cloud retrieval in presence of spatial cloud inhomogeneity  
37 even with limited independent validation data. The other two applications show how airborne measured  
38 irradiance data can be used to independently validate imagery-derived cloud products via radiative closure  
39 in irradiance. This is accomplished by simulating downwelling irradiance from geostationary cloud  
40 retrievals of Advanced Himawari Imager (AHI) along all the below-cloud aircraft flight tracks of the Cloud,  
41 Aerosol and Monsoon Processes Philippines Experiment (CAMP<sup>2</sup>Ex, NASA 2019), and comparing the  
42 irradiances with the collocated airborne measurements. In contrast to ~~case studies in the past~~, EaR<sup>3</sup>T  
43 facilitates the use of observations from entire field campaigns for the statistical validation of  
44 satellite-derived irradiance. From the CAMP<sup>2</sup>Ex mission, we find a low bias of 10% in the satellite-derived  
45 cloud transmittance, which we are able to attribute to a combination of the coarse resolution of the  
46 geostationary imager and 3D-RT biases. Finally, we apply a recently developed context-aware  
47 Convolutional Neural Network (CNN) cloud retrieval framework to high-resolution airborne imagery from  
48 CAMP<sup>2</sup>Ex and show that the retrieved cloud optical thickness fields lead to better 3D radiance consistency  
49 than the heritage independent pixel algorithm, opening the door to future mitigation of 3D-RT cloud  
50 retrieval biases.

Deleted: -

Deleted: -

Deleted: isolated

Deleted: -

55 **1. Introduction**

56 Three-dimensional cloud effects in imagery-derived cloud properties have long been  
57 considered an unavoidable error source when estimating the radiative effect of clouds and aerosols.  
58 Consequently, research efforts involving satellite, aircraft, and surface observations in conjunction  
59 with modeled clouds and radiative transfer calculations have focused on systematic bias  
60 quantification under different atmospheric conditions. Barker and Liu (1995) studied the so-called  
61 independent pixel approximation (IPA) bias in cloud optical thickness (COT) retrievals from  
62 shortwave cloud reflectance. The bias arises when approximating the radiative transfer relating to  
63 COT and measured reflectance at the pixel or cloud column level through one-dimensional (1D)  
64 radiative transfer (RT) calculations, while ignoring its radiative context. However, net horizontal  
65 photon transport and other effects such as shading engender column-to-column radiative  
66 interactions that can only be captured in a three-dimensional (3D) framework, and can be regarded  
67 as a 3D perturbation or bias relative to the 1D-RT (IPA) baseline. 3D biases affect not only cloud  
68 remote sensing but they also propagate into the derived irradiance fields and cloud radiative effects  
69 (CRE). Since the derivation of regional and global CRE relies heavily on satellite imagery, any  
70 systematic 3D bias impacts the accuracy of the Earth's radiative budget. Likewise, imagery-based  
71 aerosol remote sensing in the vicinity of clouds can be biased by net horizontal photon transport  
72 (Marshak et al., 2008). Additionally, satellite shortwave spectroscopy retrievals of CO<sub>2</sub> mixing  
73 ratio are affected by nearby clouds (Massie et al., 2017), albeit through a different physical  
74 mechanism than in aerosol and cloud remote sensing (Chen et al., 2023).

75 Given the importance of 3D perturbations for atmospheric remote sensing, ongoing  
76 research seeks to mitigate the 3D effects. Cloud tomography, for example, inverts multi-angle  
77 radiances to infer the 3D cloud extinction distribution (Levis et al., 2020). This is achieved through  
78 iterative adjustments to the cloud field until the calculated radiances match the observations.  
79 Convolutional neural networks (CNNs, Masuda et al., 2019; Nataraja et al., 2022) account for  
80 3D-RT perturbations in COT retrievals through pattern-based machine learning that operates on  
81 collections of imagery pixels, rather than treating them in isolation like IPA. Unlike tomography,  
82 CNNs require training based on extensive cloud-type specific synthetic data with the ground truth  
83 of cloud optical properties and their associated radiances from 3D-RT calculations. Once the  
84 CNNs are trained, they do not require real-time 3D-RT calculations and can therefore be useful in  
85 an operational setting. Whatever the future may hold for context-aware multi-pixel or multi-sensor

Deleted: Schmidt

Deleted: 2022

88 cloud retrievals, there is a paradigm shift on the horizon that started when the radiation concept  
89 for the Earth Clouds, Aerosol and Radiation Explorer (EarthCARE, Illingworth et al., 2015) was  
90 first proposed (Barker et al., 2012). It foresees a closure loop where broadband radiances, along  
91 with irradiance, are calculated in a 3D-RT framework from multi-sensor input fields (Barker et al.,  
92 2011), and subsequently compared to independent observations by radiometers pointing in three  
93 directions (nadir, forward-, and backward-viewing along the orbit). This built-in radiance closure  
94 can serve as an accuracy metric for any downstream radiation products such as heating rates and  
95 CRE. Any inconsistencies can be used to nudge the input fields towards the truth in subsequent  
96 loop iterations akin to optimal estimation, or propagated into uncertainties of the cloud and  
97 radiation products.

98 This general approach to radiative closure is also being considered for the National  
99 Aeronautics and Space Administration (NASA) Atmospheric Observation System (AOS,  
100 developed under the A-CCP, Aerosol and Cloud, Convection and Precipitation study), a mission  
101 that is currently in its early implementation stages. Owing to its focus on studying  
102 aerosol-cloud-precipitation-radiation interactions at the process level, it requires radiation  
103 observables at a finer spatial resolution than achieved with missions to date. At target scales close  
104 to 1 km, 3D-RT effects are much more pronounced than at the traditional 20 km scale of NASA  
105 radiation products (O’Hirok and Gautier, 2005; Ham et al., 2014; Song et al., 2016; Gristey et al.,  
106 2020a). Since this leads to biases beyond the desired accuracy of the radiation products, mitigation  
107 of 3D-RT cloud remote sensing biases needs to be actively pursued over the next few years.

108 Transitioning to an explicit treatment of 3D-RT in operational approaches entails a new  
109 generation of code architectures that can be easily configured for various instrument constellations,  
110 interlink remote sensing parameters with irradiances, heating rates, and other radiative effects, and  
111 can be used for automated processing of large data quantities. A number of 3D solvers are available  
112 for different purposes, for example, the I3RC (International Intercomparison of 3D Radiation  
113 Codes: Cahalan et al., 2005) community Monte Carlo code<sup>1</sup>, which now also includes an online  
114 simulator<sup>2</sup> ~~that was described in Várnai et al. (2022) and used in Gatebe et al. (2021)~~; MCAraTS  
115 (Monte Carlo Atmospheric Radiative Transfer Simulator<sup>3</sup>: Iwabuchi, 2006); MYSTIC (Monte

Deleted: (Gatebe et al., 2021)

<sup>1</sup> <https://earth.gsfc.nasa.gov/climate/model/i3rc>, last accessed on 26 November, 2022.

<sup>2</sup> <http://i3resimulator.umbc.edu>, last accessed on 26 November, 2022.

<sup>3</sup> <https://sites.google.com/site/mcarats/monte-carlo-atmospheric-radiative-transfer-simulator-mcarats>, last accessed on 26 November, 2022.



117 Carlo code for the physically correct tracing of photons in cloudy atmospheres: Mayer, 2009),  
118 which is embedded in libRadtran (library for radiative transfer, Mayer and Kylling, 2005);  
119 McSCIA (Monte Carlo [RT] for SCIAMachy: Spada et al., 2006), which is optimized for satellite  
120 radiance simulations (including limb-viewing) in a spherical atmosphere; McARTIM  
121 (Deutschmann et al., 2011), with several hyperspectral polarimetric applications such as  
122 differential optical absorption spectroscopy; and SHDOM (Spherical Harmonic Discrete Ordinate  
123 Method<sup>4</sup>: Evans, 1998), which, unlike the other methods, is a deterministic solver with polarimetric  
124 capabilities (Doicu et al., 2013; Emde et al., 2015) that is differentiable and can therefore be used  
125 for tomography (Loveridge et al., 2022).

126 For the future operational application of 3D-RT, it is, however, desirable to run various  
127 different solvers in one common architecture that automates the processing of various formats of  
128 3D atmospheric input fields (including satellite data), allows the user to choose from various  
129 options for atmospheric absorption and scattering, and simulates radiance and irradiance data for  
130 real-world scenes. Here, we introduce one such tool that could serve as the seed for this architecture:  
131 the Education and Research 3D Radiative Transfer Toolbox (EaR<sup>3</sup>T, pronounced [3:1]). It has been  
132 developed over the past few years at the University of Colorado to automate 3D-RT calculations  
133 based on imagery or model cloud fields, It can be operated in two ways– 1) with minimal user  
134 input, where certain RT parameters are bypassed through default settings, for quick radiation  
135 conceptual analysis; 2) with detailed RT parameters setup by user for radiation closure purpose.  
136 EaR<sup>3</sup>T is maintained and extended by graduate students as part of their education, and applied to  
137 various different research projects including machine learning for atmospheric radiation and  
138 remote sensing (Gristey et al., 2020b; 2022; Nataraja et al., 2022), as well as radiative closure and  
139 satellite simulators (this paper and Chen et al., 2023). It is implemented as a modularized Python  
140 package with various application codes that combine the functionality in different ways, which,  
141 once set up, autonomously process large amounts of data required by airborne and satellite remote  
142 sensing and for machine learning applications.

143 The goal of the paper is to introduce EaR<sup>3</sup>T as a versatile tool for systematically quantifying  
144 and mitigating 3D cloud effects in radiation science as foreseen in future missions. To do so, we  
145 will first showcase EaR<sup>3</sup>T as an automated radiance simulator for two satellite instruments, the  
146 Orbiting Carbon Observatory-2 (OCO-2, application code 1, App. 1) and the Moderate Resolution

Deleted: with minimal user input

Deleted: Schmidt

Deleted: 2022

Deleted: this application is referred to as App. 1 in this manuscript

<sup>4</sup> <https://coloradolinux.com/shdom>, last accessed on 26 November, 2022.

152 Imaging Spectroradiometer (MODIS, application code 2, App. 2) from publicly available satellite  
153 retrieval products. In the spirit of radiance closure, the intended use is the comparison of modeled  
154 radiances with the original measurements to assess the accuracy of the input data, as follows:  
155 operational IPA COT products are made using 1D-RT, and thus the accompanying radiances are  
156 consistent with the original measurements under that 1D-RT assumption only. That is,  
157 self-consistency is assured if 1D-RT is used in both the inversion and radiance simulation.  
158 However, since nature creates 3D-RT radiation fields, we break this traditional symmetry in this  
159 manuscript and introduce the concept of 3D radiance consistency where closure is only achieved  
160 if the original measurements are consistent with the 3D-RT (rather than the 1D-RT) simulations.  
161 The level of inconsistency is then used as a metric for the magnitude of 3D-RT retrieval artifacts  
162 as envisioned by the architects of the EarthCARE radiation concept (Barker et al., 2012).

163 Subsequently, we discuss applications where EaR<sup>3</sup>T performs radiative closure in the  
164 traditional sense, i.e., between irradiances derived from satellite products and collocated airborne  
165 or ground-based observations. The aircraft Cloud, Aerosol and Monsoon Processes Philippines  
166 Experiment (CAMP<sup>2</sup>Ex, Reid et al., 2023), conducted by NASA in the Philippines in 2019, serves  
167 as a testbed of this approach. Here, we use EaR<sup>3</sup>T's automated processing capabilities to derive  
168 irradiance from geostationary imagery cloud products and then compare these to cumulative  
169 measurements made along all flight legs of the campaign (application code 3, App. 3). In contrast  
170 to previous studies that often rely on a number of cases (e.g., Schmidt et al., 2010; Kindel et al.,  
171 2010), we perform closure systematically for the entire data set, enabling us to identify 3D-RT  
172 biases in a statistically significant manner. Finally, we apply a regionally and cloud type specific  
173 CNN, introduced by Nataraja et al. (2022) that is included with the EaR<sup>3</sup>T distribution, to  
174 high-resolution camera imagery from CAMP<sup>2</sup>Ex. This last example demonstrates mitigation of  
175 3D-RT biases in cloud retrievals using the concept of radiance closure to quantify its performance  
176 against the baseline IPA (application code 4, App. 4).

177 The general concept of EaR<sup>3</sup>T with an overview of the applications, along with the data  
178 used for both parts of the paper is presented in section 2, followed by a description of the  
179 procedures of EaR<sup>3</sup>T in section 3. Results for the OCO-2 and MODIS satellite simulators (part 1)  
180 are shown in section 4, followed by the quantification and mitigation of 3D-RT biases with  
181 CAMP<sup>2</sup>Ex data in section 5 and section 6 (part 2). A summary and conclusion are provided in

Deleted: -

Deleted: 2022

Deleted: -

185 section 7. The code, along with the applications presented in this paper, can be downloaded from  
 186 the GitHub repository: <https://github.com/hong-chen/er3t>.

187

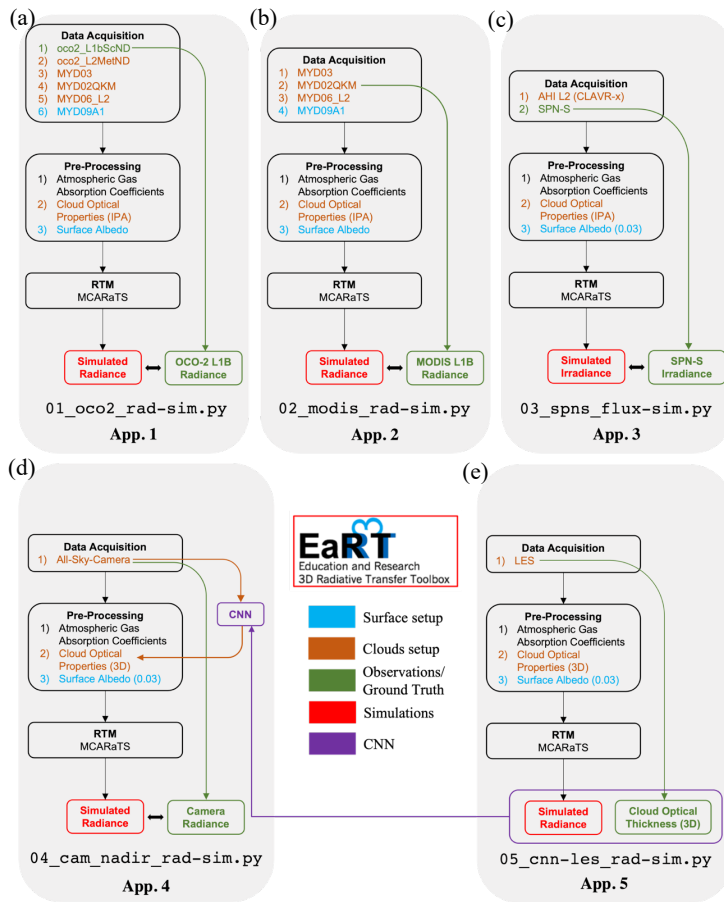
188 **2. Functionality and Data Flow within EaR<sup>3</sup>T**

189 **2.1 Overview**

190 To introduce EaR<sup>3</sup>T as a satellite radiance simulator tool and to demonstrate its use for the  
 191 quantification and mitigation of 3D cloud remote sensing biases, five applications (Figure 1) are  
 192 included in the GitHub software release;

Deleted: , four of which are discussed in this paper

193



194

196 **Figure 1.** Flow charts of EaR<sup>3</sup>T applications for (a) OCO-2 radiance simulation at 768.52 nm (data described in section  
197 2.2.1 and 2.2.2, results discussed in section 4.1), (b) MODIS radiance simulation at 650 nm (data described  
198 in section 2.2.1, results discussed in section 4.2), (c) SPN-S irradiance simulation at 745 nm (data described  
199 in section 2.2.3 and 2.2.4, results discussed in section 5), (d) all-sky camera radiance simulation at 600 nm  
200 (data described in section 2.2.5, results discussed in section 6), and (e) radiance simulation at 600 nm based  
201 on LES data for CNN training (Appendix B). The data products and their abbreviations are described in  
202 section 2.2.

203

- 204 1. App. 1, section 4.1 (`examples/01_oco2_rad-sim.py`): Radiance simulations along  
205 the track of OCO-2, based on data products from MODIS and others – to assess consistency  
206 (closure) between simulated and measured radiance;
- 207 2. App. 2, section 4.2 (`examples/02_modis_rad-sim.py`): MODIS radiance  
208 simulations – to assess self-consistency of MODIS level-2 (L2) products with the  
209 associated radiance fields (L1B product) under spatially inhomogeneous conditions;
- 210 3. App. 3, section 5 (`examples/03_spns_flux-sim.py`): Irradiance simulations along  
211 aircraft flight tracks, utilizing the L2 cloud products of the AHI, and comparison with  
212 aircraft measurements – to quantify retrieval biases due to 3D cloud structure based with  
213 data from an entire aircraft field campaign;
- 214 4. App. 4, section 6 (`examples/04_cam_nadir_rad-sim.py`): Mitigation of 3D  
215 cloud biases in passive imagery COT retrievals from an airborne camera, application of a  
216 convolutional neural network (CNN) and subsequent comparison of CNN-derived  
217 radiances with the original measurements – to illustrate how the radiance self-consistency  
218 concept assesses the fidelity of cloud retrievals.
- 219 5. App. 5, Appendix B (`examples/05_cnn-les_rad-sim.py`): Generation of training  
220 data for the CNN (App. 4) based on LES inputs. The training datasets contains 1) the  
221 ground truth of COT from the LES data; 2) realistic radiance simulated by EaR<sup>3</sup>T based on  
222 the LES cloud fields.

223 Figure 1 shows the high-level workflow of the applications. The first four share the general  
224 concept of evaluating simulations (the output from the EaR<sup>3</sup>T, indicated in red at the bottom of  
225 each column) with observations (indicated in green at the bottom) from various satellite and  
226 aircraft instruments. The workflow of each application consists of three parts – 1) data acquisition,  
227 2) pre-processing, and 3) RTM setup and execution. EaR<sup>3</sup>T includes functions to ingest data from

Deleted: 4

Deleted: 4

Deleted: The results for the first four applications are interpreted in section 4.1, section 4.2, section 5, and section 6. The results for App. 5 are discussed in detail in a separate paper by Nataraja et al. (2022). In this paper, we will only provide a brief description for App. 5 in Appendix B.

235 various different sources, e.g., satellite data from publicly available data archives, which can be  
236 combined in different ways to accommodate input data depending on the application specifics. For  
237 example, in App. 1, EaR<sup>3</sup>T is used to automatically download and process MODIS and OCO-2  
238 data files based on the user-specified region, date and time. Building on the templates provided in  
239 the current code distribution, the functionality can be extended to new spaceborne or airborne  
240 instruments. Panel (e) of Figure 1 shows a fifth application that was developed for earlier papers  
241 (Gristey et al., 2020a and 2020b; Nataraja et al., 2022; Gristey et al., 2022). In contrast to the first  
242 four, which use imagery products as input, the fifth application ingests model output from a Large  
243 Eddy Simulation (LES) and produces irradiance data for surface energy budget applications, or  
244 synthetic radiance fields for training a CNN. Details and results are described in the respective  
245 papers. The remainder of Section 2 introduces the data used in this paper, as well as the input for  
246 EaR<sup>3</sup>T. Subsequently, Section 3 describes the EaR<sup>3</sup>T procedures.

## 248 2.2 Data

249 The radiance simulations in App. 1 and App. 2 use data from the OCO-2 and MODIS-Aqua  
250 instruments, both of which are in a sun-synchronous polar orbit with an early-afternoon equator  
251 crossing time within NASA's A-Train satellite constellation. Figure 2 visualizes radiance  
252 measurements by OCO-2 in the context of MODIS Aqua imagery over a partially vegetated and  
253 partially cloud-covered land, illustrating that MODIS provides imagery and scene context for  
254 OCO-2, which in turn observes radiances from a narrow swath. The region is located in southwest  
255 Colorado in the United States of America. We selected this case because both the surface and  
256 clouds are varied along with diverse surface types. The surface features green forest and brown  
257 soil, whereas clouds include small cumulus and large cumulonimbus. In addition, this scene  
258 contains relatively homogeneous cloud fields in the north and inhomogeneous cloud fields in the  
259 south, which allows us to evaluate the simulations from various aspects of cloud morphology. To  
260 simulate the radiances of both instruments we use data products from OCO-2 and MODIS, as well  
261 as reanalysis products from NASA's Global Modeling and Assimilation Office (GMAO) sampled  
262 at OCO-2 footprints and distributed along with OCO-2 data (section 2.2.2).

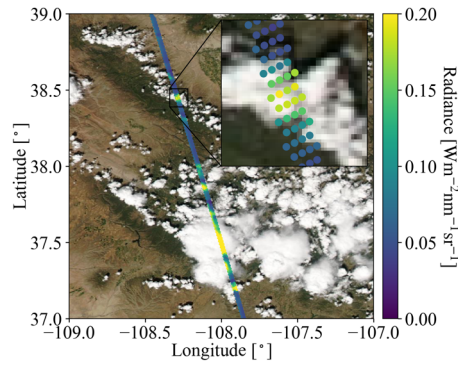
**Deleted:** The fifth column

**Deleted:** an application that differs from the first four, and

**Deleted:** Furthermore, Schmidt et al. (2022) builds upon App. 1 to study the mechanism of 3D cloud biases in OCO-2 passive spectroscopy retrievals.

**Deleted:** → After the required data files have been downloaded in the data acquisition step, EaR<sup>3</sup>T pre-processes them and generates the optical properties of atmospheric gases, clouds, aerosols, and the surface. In Figure 1, the mapping from input data to these properties is color-coded component-wise (brown for associated cloud property processing if available, blue for associated surface property processing if available, green for associated ground truth property). The version used in this paper (v0.1.0; Chen and Schmidt, 2022) only includes MCARaTS as the 3D RT solver, but others are planned for the future. MCARaTS is a radiative transfer solver uses Monte Carlo photon-tracing method (Iwabuchi, 2006). It outputs radiation (radiance or irradiance) based on the inputs of radiative properties of surface and atmospheric constituents (e.g., gases, aerosols, clouds) such as single scattering albedo, scattering phase function, or asymmetry parameters, along with solar and sensor viewing geometries. The setup of these input properties is implemented in EaR<sup>3</sup>T's pre-processing steps, which translates atmospheric properties into solver-specific input with minimum user intervention. To achieve this, EaR<sup>3</sup>T is modular so that it can be extended as new solvers are added. Although the five specific applications in this paper do not include aerosol layers, the setup of aerosol fields is fully supported and has been used in other applications (e.g., Gristey et al., 2022). After pre-processing, the optical properties are fed into the RT solver. Finally, the user obtains radiation output from EaR<sup>3</sup>T, either radiance or irradiance. The output is saved in HDF5 format and can be easily distributed and accessed by various programming languages. The data variables contained in the HDF5 output are provided in Table 1.¶

The aforementioned three steps – data acquisition, pre-processing, and RTM setup and execution are automated such that the 3D/1D-RT calculations can be performed for any region at any date and time using satellite or aircraft data or other data resources such as LES. EaR<sup>3</sup>T is hosted on GitHub at <https://www.github.com/hong-chen/er3t>. Since it is developed as an educational and research 3D-RT tool collection by students, it is a living code base, intended to be updated over time. The master code modules for the five applications as listed in Figure 1 are included in the EaR<sup>3</sup>T package under the `examples` directory. In the current release (v0.1.0), only a limited documentation for the installation and usage, including example codes for EaR<sup>3</sup>T, are provided. More effort will be dedicated for documentation in the near-future.¶



316  
 317 **Figure 2.** OCO-2 measured radiance (units:  $\text{Wm}^{-2}\text{nm}^{-1}\text{sr}^{-1}$ ) at 768.52 nm, overlaid on MODIS Aqua RGB imagery  
 318 over southwestern Colorado (USA) on 2 September, 2019. The inset shows an enlarged portion along the  
 319 track, illustrating that OCO-2 radiances co-vary with MODIS-Aqua radiance observations (the circles are  
 320 used to indicate the geolocation of OCO-2 footprints).

321  
 322 For App. 3 (irradiance simulations and 3D cloud bias quantification), we use geostationary  
 323 imagery from the Japanese Space Agency’s Advanced Himawari Imager to provide cloud  
 324 information in the area of the flight path of the NASA CAMP<sup>2</sup>Ex aircraft (Reid et al., 2023). The  
 325 AHI data are used in conjunction with aircraft measurements of shortwave spectral radiation  
 326 (section 2.2.4). Subsequently (App. 4: 3D cloud bias mitigation), we demonstrate the concept of  
 327 radiance closure under partially cloudy conditions with airborne camera imagery (section 2.2.5).  
 328 The underlying cloud retrieval is based on a convolutional neural network (CNN), which is  
 329 described in a related paper (Nataraja et al., 2022) in this special issue and relies on  
 330 EaR<sup>3</sup>T-generated synthetic radiance data based on Large Eddy Simulations (LES).

Deleted: 2022

331  
 332 **2.2.1 Moderate Resolution Imaging Spectroradiometer (MODIS)**

333 The MODIS instruments are multi-use multispectral radiometers onboard NASA’s Terra  
 334 and Aqua satellites, which were launched in 1999 and 2002 respectively. MODIS was conceived  
 335 as a central element of the Earth Observing System (EOS, King and Platnick, 2018). For App. 1  
 336 and App. 2, EaR<sup>3</sup>T ingests MODIS level 1B radiance products at the quarter kilometer scale  
 337 (channels 1 and 2, bands centered at 650 and 860 nm), MxD02QKM, where ‘x’ stands for ‘O’ in  
 338 the case of MODIS on Terra, and ‘Y’ in the case of Aqua data), the geolocation product (MxD03),  
 339 the level 2 cloud product (MxD06), and the surface BRDF (bidirectional reflectance distribution

Deleted: -

Deleted: reflectance

343 function) product (MCD43A3). For this paper, we mainly use Aqua data (MYD) from data  
344 collection 6.1.

345 For cloud properties in App. 2, we use the MODIS cloud product (MxD06L2, collection  
346 6.1). It provides cloud properties such as cloud optical thickness (COT), cloud effective radius  
347 (CER), cloud thermodynamic phase, cloud top height (CTH), etc. (Nakajima and King, 1990;  
348 Platnick et al., 2003). Since 3D cloud effects such as horizontal photon transport are most  
349 significant at small spatial scales (e.g., Song et al., 2016), we use the high-resolution red (650 nm)  
350 channel 1 (250 m), and derive COT directly from the reflectance in the Level-1B data  
351 (MYD02QKM) instead of using the coarser-scale operational product from MYD06. CER and  
352 CTH are sourced from MYD06 and re-gridded to 250 m. The EaR<sup>3</sup>T strategy for MODIS data is  
353 similar, in principle, to the more advanced method by Deneke et al. (2021), which uses a  
354 high-resolution wide-band visible channel from geostationary imagery to up-sample narrow-band  
355 coarse-resolution channels. However, we simplified cloud detection and COT retrieval (referred  
356 to as COT<sub>IPA</sub>) from reflectance data for the purpose of our paper by using a threshold method  
357 (Appendix C1) and an IPA reflectance-to-COT mapping (Appendix C2). In future versions of  
358 EaR<sup>3</sup>T this will be upgraded to more sophisticated algorithms. A simple algorithm (Appendix D1)  
359 is used to correct for the parallax shift based on the sensor geometries and cloud heights. The cloud  
360 top height data is provided by the MODIS L2 cloud product and assuming cloud base is the same.

361 For the surface albedo required by the RTM, we used MCD43A3, which provides BRDF  
362 calculated from a combination of Aqua and Terra MODIS and MISR (Multi-Angle Imaging  
363 Spectroradiometer) clear-sky observations aggregated over a 16-day period (Strahler et al., 1999).  
364 This product contains white sky albedo (WSA, also known as bihemispherical reflectance), which  
365 is obtained by integrating the BRDF over all viewing angles (Strahler et al., 1999). The WSA is  
366 available on a sinusoidal grid with a spatial resolution of 500 m for MODIS band 2, and includes  
367 atmospheric correction for gas and aerosol scattering and absorption. Assuming a Lambertian  
368 surface in this first release of EaR<sup>3</sup>T, we used the WSA (referred to as surface albedo from now  
369 on) as surface albedo input to the RTM.

### 371 2.2.2 Orbiting Carbon Observatory 2 (OCO-2)

372 The OCO-2 satellite was inserted into NASA's A-Train constellation in 2014 and flies  
373 about 6 minutes ahead of Aqua. OCO-2 provides the column-averaged carbon dioxide (CO<sub>2</sub>)

Deleted: MxD09A1

Deleted: only

Deleted: ,

Deleted: . All the data are publicly available, and are distributed at the LAADS (Level-1 and Atmosphere Archive & Distribution System) Distributed Active Archive Center (DAAC) by NASA's Goddard Space Flight Center

Deleted: derivation of COT

Formatted: Subscript

Deleted: the

Deleted: two-stream approximation

Deleted: MYD09A1

Deleted: cloud-cleared surface reflectance observations aggregated...

Deleted: n

Deleted: 8

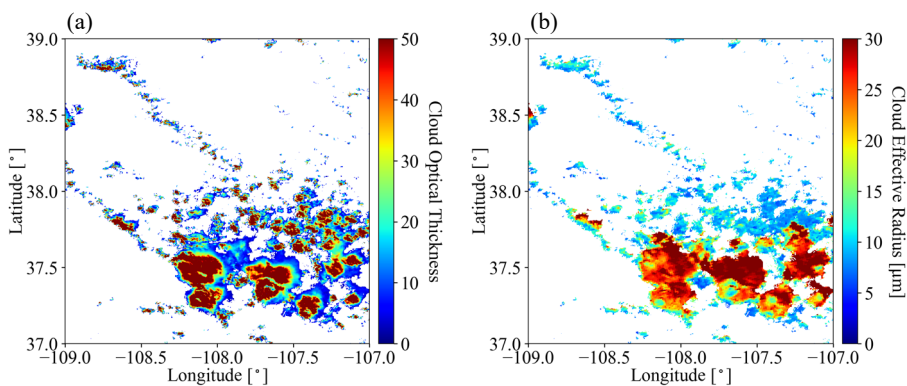
Deleted: Vermote et al., 2015

Deleted: surface reflectance

391 dry-air mole fraction ( $X_{CO_2}$ ) through passive spectroscopy based on hyperspectral radiance  
 392 observations in three narrow wavelength regions, the Oxygen A-Band ( $\sim 0.76$  micron), the weak  
 393  $CO_2$  band ( $\sim 1.60$  micron), and the strong  $CO_2$  band ( $\sim 2.06$  micron). As shown in the inset of Figure  
 394 2, it takes measurements in eight footprints across a narrow swath. Each of the footprints has a  
 395 size around 1-2 km, and the spectra for the three bands are provided by separate, co-registered  
 396 spectrometers (Crisp et al., 2015).

397 The used OCO-2 data products are 1) Level 1B calibrated and geolocated science radiance  
 398 spectra (L1bScND), 2) standard Level 2 geolocated  $X_{CO_2}$  retrievals results (L2StdND), 3)  
 399 meteorological parameters interpolated from GMAO (L2MetND) at OCO-2 footprint location.  
 400 Since MODIS on Aqua overflies a scene 6 minutes after OCO-2, the clouds move with the wind  
 401 over this time period. We therefore added a wind correction on top of the parallax-corrected cloud  
 402 fields obtained from MODIS (section 2.2.1). This was done with the 10 m wind speed data from  
 403 L2MetND (see Appendix D2). For the same scene as shown in Figure 2, Figure 3 shows (a) COT<sub>IPA</sub>,  
 404 (b) CER, and (c) CTH, all corrected for both parallax and wind effects (these corrections are shown  
 405 in Figure A5 in Appendix D2). The parallax and wind corrections are imperfect as certain  
 406 assumptions are involved. For example, they rely on the cloud top height from the MODIS cloud  
 407 product. In addition, they process the whole scene with one single sensor viewing geometry. To  
 408 minimize artifacts introduced by the assumptions, one can apply the simulation to a smaller region.

409  
 410



411

Deleted: of

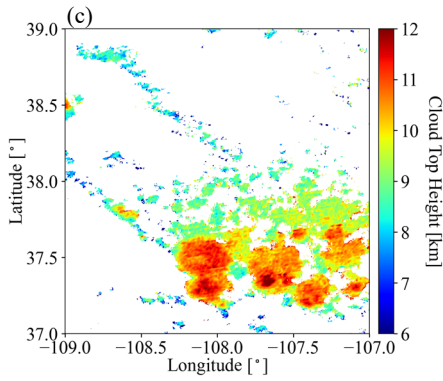
Deleted: are downloaded from NASA GES DISC (Goddard Earth Science Data Archive and Information Services Center) data archive ([https://oco2.gesdisc.cosdis.nasa.gov/data/OCO2\\_DATA](https://oco2.gesdisc.cosdis.nasa.gov/data/OCO2_DATA))

Formatted: Subscript

Deleted: A2

Deleted: D





419  
 420 **Figure 3.** (a) Cloud optical thickness derived from MODIS L1B radiance at 650 nm by the [IPA reflectance-to-COT](#)  
 421 [mapping \(Appendix C2\)](#), (b) cloud effective radius (units:  $\mu\text{m}$ ), and (c) cloud top height (units: km)  
 422 collocated from the MODIS L2 cloud product. The locations of the cloudy pixels were shifted to account  
 423 for parallax and wind effects. The parallax correction ranged from near 0 for low clouds and 1 km for high  
 424 clouds (10 km CTH). The wind correction was around 0.8 km, given the [median](#) wind speed of 2 m/s to the  
 425 east.

426  
 427 The OCO-2 data (L2StdND) themselves only provide sparse [surface BRDF \(referred to as](#)  
 428 [surface albedo from now on\)](#) for the footprints that are clear, while EaR<sup>3</sup>T requires surface albedo  
 429 for the whole domain. Therefore, we used [MCD43A3](#) as a starting point. However, since MODIS  
 430 does not have a channel in the Oxygen A-Band, MODIS band 2 (860 nm) was used as a proxy for  
 431 the 760 nm OCO-2 channel as follows: we collocated the OCO-2 retrieved 760 nm [surface albedo](#)  
 432  $\alpha_{OCO}$  within the corresponding 860 nm MODIS [MCD43A3](#) data  $\alpha_{MOD}$ , as shown in Figure 4a  
 433 (same domain as Figures 2 and 3) and calculated a scaling factor assuming a linear relationship  
 434 between  $\alpha_{OCO}$  and  $\alpha_{MOD}$  ( $\alpha_{OCO} = c \cdot \alpha_{MOD}$ ). Figure 4b shows  $\alpha_{OCO}$  versus  $\alpha_{MOD}$  for all  
 435 cloud-free OCO-2 footprints. The red line shows a linear regression (derived scale factor  $c=0.867$ ).  
 436 Optionally, the OCO-2-scaled MODIS-derived [surface albedo](#) fields can be replaced by the OCO-2  
 437 [surface albedo](#) products for pixels where they are available. [The replacement is done for App. 1.](#)  
 438 The scaled [and replaced surface albedo](#) is then treated as input to the RTM assuming a Lambertian  
 439 surface.

Deleted: two-stream approximation

Deleted: Eq. A2

Deleted: average

Deleted: surface reflectance

Deleted: MYD09A1

Deleted: surface reflectance

Deleted:  $R_{OCO}$

Deleted: MYD09A1

Deleted:  $R_{MOD}$

Deleted:  $R_{OCO}$

Deleted:  $R_{MOD}$

Deleted:  $R_{OCO} = a \cdot R_{MOD}$

Deleted:  $R_{OCO}$

Deleted:  $R_{MOD}$

Deleted: -

Deleted:  $a=0.93$

Deleted: surface reflectance

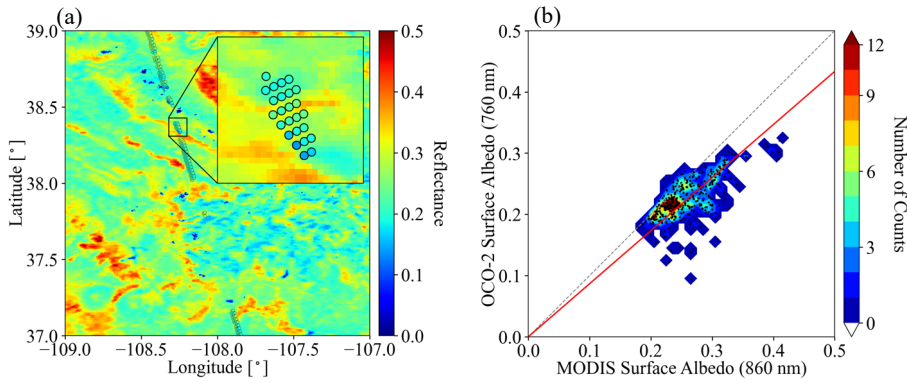
Deleted: -

Deleted: surface

Deleted: reflectance

Deleted: surface reflectance

Deleted: surface albedo



463  
464 **Figure 4.** (a) Surface albedo from the OCO-2 L2 product in the Oxygen A-band (near 760 nm), overlaid on the surface  
465 albedo from the MODIS MCD43A3 product at 860 nm. (b) OCO-2 surface albedo at 760 nm versus MODIS  
466 surface albedo at 860 nm, along with linear regression ( $\alpha_{OCO} = c \cdot \alpha_{MODIS}$ ) as indicated by the red line (slope  
467  $c=0.867$ ).

### 469 2.2.3 Advanced Himawari Imager (AHI)

470 The Advanced Himawari Imager (AHI, used for App. 3) is a payload on Himawari-8, a  
471 geostationary satellite operated by the Meteorological Satellite Center (MSC) of the Japanese  
472 Meteorological Agency. The AHI provides 16 channels of spectral radiance measurements from  
473 the shortwave (0.47 $\mu$ m) to the infrared (13.3 $\mu$ m). During CAMP<sup>2</sup>Ex, the NASA in-field  
474 operational team closely collaborated with the team from MSC to provide AHI satellite imagery  
475 at the highest resolution over the Philippine Sea. From the AHI imagery, the cloud product  
476 generation system - Clouds from AVHRR Extended System (CLAVR-x), was used to generate  
477 cloud products from the AHI imagery (Heidinger et al., 2014). The cloud products from CLAVR-x  
478 include cloud optical thickness, cloud effective radius, and cloud top height at 2 (at nadir) to 5 km  
479 spatial resolution. Since AHI provides continuous regional scans every 10 minutes the AHI cloud  
480 product has a temporal resolution of 10 minutes.

### 482 2.2.4 Spectral Sunshine Pyranometer (SPN-S)

483 The SPN-S is a prototype spectral version of the commercially available global-diffuse  
484 SPN1 pyranometer (Wood et al., 2017; Norgren et al., 2022). The radiometer uses a 7-detector  
485 design in combination with a fixed shadow mask that enables the simultaneous measurement of  
486 both diffuse and global irradiances, from which the direct component of the global irradiance is

- Deleted: reflectance
- Deleted: surface reflectance
- Deleted: MYD09
- Deleted: surface reflectance
- Deleted: surface reflectance
- Deleted:  $y=ax$
- Deleted:  $a$
- Deleted: 0.9337

Deleted: -

496 calculated via subtraction. The detector measures spectral irradiance from 350 to 1000 nm, and the  
497 spectrum is sampled at 1 nm resolution with 1 Hz timing.

498 During the CAMP<sup>2</sup>Ex mission, the SPN-S was mounted to the top of the NASA P-3 aircraft  
499 where it sampled downwelling solar irradiance. To ensure accurate measurements, pre- and  
500 post-mission laboratory-based calibrations were completed using tungsten “FEL” lamps that are  
501 traceable to a National Institute of Standards and Technology standard. Additionally, the direct  
502 and global irradiances were corrected for deviations of the SPN-S sensor plane from horizontal  
503 that are the result of changes in the aircraft’s pitch or roll. This attitude correction applied to the  
504 irradiance data is a modified version of the method outlined in Long et al. (2010). However,  
505 whereas Long et al. (2010) employ a “box” flight pattern to characterize the sensor offset angles,  
506 in this study an aggregation of flight data containing aircraft heading changes under clear-sky  
507 conditions are used as a substitute. The estimated uncertainty of the SPN-S system is 6 to 8%, with  
508 4 to 6% uncertainty stemming from the radiometric lamp calibration process, and up to another 2%  
509 resulting from insufficient knowledge of the sensor cosine response. The stability of the system  
510 under operating conditions is 0.5%. A thorough description of the SPN-S and its calibration and  
511 correction procedures is provided in Norgren et al. (2022). In this paper (App. 3) only the global  
512 downwelling irradiance sampled by the 745 nm channel is used.

513

#### 514 **2.2.5 Airborne All-Sky Camera (ASC)**

515 The All-Sky Camera (used for App. 4) is a commercially available camera (ALCOR  
516 ALPHEA 6.0CW<sup>5</sup>) with fish-eye optics for hemispheric imaging. It has a Charge-Coupled Device  
517 (CCD) detector that measures radiances in red, green, and blue channels. Radiometric and  
518 geometric calibrations were performed at the Laboratory of Atmospheric and Space Physics at the  
519 University of Colorado Boulder. The three-color channels are centered at 493, 555, and 626 nm  
520 for blue, green, and red, respectively, with bandwidths of 50 – 100 nm. Only radiance data from  
521 the red channel are used in this paper. The spatial resolution of the ASC depends on the altitude of  
522 the aircraft and the viewing zenith angle. Across the hemispheric field of view of the camera, the  
523 resolution of the field angle is approximately constant, at about 0.09°. At a flight level of 5 km,

Deleted: -

---

<sup>5</sup>[https://www.alcor-system.com/common/allSky/docs/ALPHEA\\_Camera%20ALL%20SKY%20CAMERA\\_Doc.pdf](https://www.alcor-system.com/common/allSky/docs/ALPHEA_Camera%20ALL%20SKY%20CAMERA_Doc.pdf)  
last accessed on April 24, 2022.

525 this translates to a spatial resolution of 8 m at nadir. However, due to accuracy limitations of the  
526 geometric calibration and the navigational data from Inertial Navigation System (INS), the nadir  
527 geolocation accuracy could only be verified to within  $\pm 50$  m. During the CAMP<sup>2</sup>Ex flights, the  
528 camera exposure time was set manually to minimize saturation of the detector. The standard image  
529 frame rate is 1 Hz. The precision of the camera radiances is on the order of 1%, and the radiometric  
530 accuracy is 6 – 7%.

531

### 532 3. EaR<sup>3</sup>T Procedures

533 ~~In the previous section, we described the input data for the EaR<sup>3</sup>T applications. In this~~  
534 ~~section, we will focus on providing the complete workflow (shown in Figure 1) for the five~~  
535 ~~applications.~~

536 After the required data files have been automatically downloaded in the data acquisition  
537 step as described in previous section, EaR<sup>3</sup>T pre-processes them and generates the optical  
538 properties of atmospheric gases, clouds, aerosols, and the surface. In Figure 1, the mapping from  
539 input data to these properties is color-coded component-wise (brown for associated cloud property  
540 processing if available, blue for associated surface property processing if available, green for  
541 associated ground truth property). The EaR<sup>3</sup>T code base used in this paper (v0.1.1; Chen and  
542 Schmidt, 2022) only includes MCARaTS as the 3D RT solver, but others are planned for the future.  
543 MCARaTS is a radiative transfer solver that uses a Monte Carlo photon-tracing method (Iwabuchi,  
544 2006). It outputs radiation (radiance or irradiance) based on the inputs of radiative properties of  
545 surface and atmospheric constituents (e.g., gases, aerosols, clouds) such as single scattering albedo,  
546 scattering phase function or asymmetry parameter, along with solar and sensor viewing geometries.  
547 The setup of these input properties is implemented in EaR<sup>3</sup>T's pre-processing steps, which  
548 translates atmospheric properties into solver-specific input with minimum user intervention. To  
549 achieve this, EaR<sup>3</sup>T is modular so that it can be extended as new solvers are added. Although the  
550 five specific applications in this paper do not include aerosol layers, the setup of aerosol fields is  
551 fully supported and has been used in other applications (e.g., Gristey et al., 2022). After pre-  
552 processing, the optical properties are fed into the RT solver. Finally, the user obtains radiation  
553 output from EaR<sup>3</sup>T, either radiance or irradiance. The output is saved in HDF5 format and can be  
554 easily distributed and accessed by various programming languages. The data variables contained  
555 in the HDF5 output are provided in Table A2 in Appendix A1.

Moved (insertion) [2]

Deleted: general workflow

Deleted: of

Deleted: , along with relevant data

Deleted: the specific implementation of

Deleted: the

Deleted: through the

Deleted: EaR<sup>3</sup>T software package. It is a toolbox for 3D-RT with modules for automatic input data download and processing, generation of radiative and optical properties of surface, atmospheric gases, clouds and aerosols, wrappers for 3D-RT solvers and output post-processing, with the end goal to simulate radiances and irradiances along entire satellite orbits or aircraft flight tracks. Unlike established radiative transfer packages such as libRadtran (Mayer and Kylling, 2005; Emde et al., 2016), which provide extensive libraries of optical properties along with a selection of solvers, EaR<sup>3</sup>T focuses on automated radiative transfer for two- or three-dimensional cloud, aerosol, and surface input data, and therefore only comes with minimal options for optical properties, and solvers.

576 The processes of data acquisition, pre-processing, and RTM setup and execution (shown  
577 in Figure 1) are automated such that the 3D/1D-RT calculations can be performed for any region  
578 at any date and time using satellite or aircraft data or other data resources such as LES. A detailed  
579 code walk-through of App. 1 and 2 is provided in Appendix A2. Since EaR<sup>3</sup>T is developed as an  
580 educational and research 3D-RT tool collection by students, it is a living code base, intended to be  
581 updated over time. The master code modules for the five applications as listed in Figure 1 are  
582 included in the EaR<sup>3</sup>T package under the `examples` directory. In the current release (v0.1.1),  
583 only a limited documentation for the installation and usage, including example code for EaR<sup>3</sup>T, is  
584 provided. More effort will be dedicated for documentation in the near-future.

585 In the following sections, we discuss results obtained from EaR<sup>3</sup>T, starting with those from  
586 `examples/01_oco2_rad-sim.py` and `examples/02_modis_rad-sim.py` (section  
587 4), `examples/03_spns_flux-sim.py` (section 5), and concluding with  
588 `examples/04_cam_nadir_rad-sim.py` (section 6). The usage of the EaR<sup>3</sup>T package  
589 including the technical input and output parameters and code walk-through is provided in  
590 Appendix A.

#### 592 4. EaR<sup>3</sup>T as a 3D Satellite Radiance Simulator

593 This section demonstrates the automated 3D radiance simulation for satellite instruments  
594 by EaR<sup>3</sup>T for OCO-2 and MODIS measured radiance based on publicly available MODIS retrieval  
595 products. The OCO-2 application is an example of radiance consistency between two distinct  
596 satellite instruments where the measurements of one (here, OCO-2) are compared with the  
597 simulations based on data products from the other (here, MODIS). The MODIS application, on  
598 the other hand, is an example of radiance self-consistency. We will show how inconsistencies can  
599 be used for detecting cloud and surface property retrieval biases.

##### 600 4.1 OCO-2 (App. 1)

601 The OCO-2 radiance measurements at 768.52 nm for our sample scene in the context of  
602 MODIS imagery were shown in Figure 2. For that track segment, Figure 5a shows the simulated  
603 radiance along with the measurements as a function of latitude. The radiance was averaged over  
604 every 0.01° latitude window from 37° N to 39° N (the standard deviation within the bin indicated  
605 by the shaded color). In clear-sky regions (e.g., around 38.2° N), the 3D simulations (red) are  
606 systematically higher than the measurements (black), even though the footprint-level OCO-2

**Moved up [2]:** In the previous section, we described the general workflow of EaR<sup>3</sup>T applications, along with relevant data. In this section, we will focus on the specific implementation of the workflow through the EaR<sup>3</sup>T software package. It is a toolbox for 3D-RT with modules for automatic input data download and processing, generation of radiative and optical properties of surface, atmospheric gases, clouds and aerosols, wrappers for 3D-RT solvers and output post-processing, with the end goal to simulate radiances and irradiances along entire satellite orbits or aircraft flight tracks. Unlike established radiative transfer packages such as libRadtran (Mayer and Kylling, 2005; Emde et al., 2016), which provide extensive libraries of optical properties along with a selection of solvers, EaR<sup>3</sup>T focuses on automated radiative transfer for two- or three-dimensional cloud, aerosol, and surface input data, and therefore only comes with minimal options for optical properties, and solvers.

**Deleted:** The initial release (version 0.1.0) is available at <https://github.com/hong-chen/er3t>.

**Moved down [1]:** In addition to MCARaTS, planned solvers for the future include MYSTIC (Monte Carlo code for the physically correct tracing of photons in cloudy atmospheres, Mayer, 2009) and SHDOM (Spherical Harmonic Discrete Ordinate Method, Evans, 1998; Pincus and Evans, 2009).

**Deleted:** After the data acquisition step, the satellite data are fed into the pre-processing step for 1) atmospheric gases (`er3t/pre/atm`), 2) clouds (`er3t/pre/cld`), 3) surface (`er3t/pre/sfc`) as shown in Figure 1. In the default configuration of the App. 1, the standard US atmosphere (Anderson et al., 1986; included in the EaR<sup>3</sup>T repository) is used within `atm`. EaR<sup>3</sup>T supports the input of user-specified atmospheric profiles, e.g., atmospheric profiles from reanalysis data for App. 2 as described in Schmidt et al. (2022), by making changes in `atm_atmmod` (from `er3t/pre/atm`). Subsequently, molecular scattering coefficients are calculated by `cal_mol_ext` (from `er3t/util`), and absorption coefficients for atmospheric gases are generated by (`er3t/pre/abs`). At the current development stage, two options are available: Line-by-line (used by App. 1): The repository includes a sample file of absorption coefficient profiles for a subset of wavelengths within OCO-2's Oxygen A-Band channel, corresponding to a range of atmospheric transmittance values from low (opaque) to high (so-called "continuum" wavelength). They were generated by an external code (Schmidt et al., 2022) based on OCO-2's line-by-line absorption coefficient database (ABSCO, Payne et al., 2020). For each OCO-2 spectrometer wavelength within a given channel, hundreds of individual absorption coefficient profiles at the native resolution of ABSCO need to be considered across the instrument line shape (ILS, also known as the slit function) of the spectrometer. The ILS, as well as the incident solar irradiance, are also included in the file. In subsequent steps, EaR<sup>3</sup>T performs RT calculations at the native spectral resolution of ABSCO, but then combines the output by convolving with the ILS and outputs OCO-2 radiances or reflectances at the subset of wavelengths. ... [1]

**Deleted:** The detailed RT setup for the applications is provided Table A1 in Appendix A

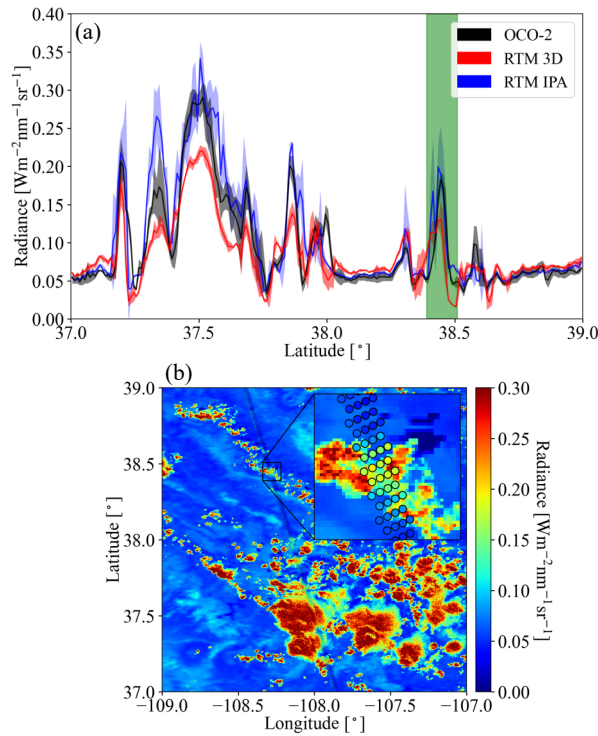
743 surface albedo retrieval was used to replace and scale the MCD43 surface albedo field as described  
 744 in section 2.2.2 (Figure 4). This is probably because, unlike the MCD43 algorithm which relies on  
 745 multiple overpasses and multiple-days for cloud-clearing, the OCO-2 retrieval is done for any clear  
 746 footprint. Clouds in the vicinity lead to enhanced diffuse illumination that is erroneously attributed  
 747 to the surface albedo itself. The EaR<sup>3</sup>T IPA calculations of the clear-sky pixels (blue) essentially  
 748 reverse the 3D effect and therefore match the observations better. The 3D calculations enhance the  
 749 reflectance through the very same 3D cloud effects that led to the enhanced surface illumination  
 750 in the first place. It is possible to correct this effect by down-scaling the surface albedo according  
 751 to the ratio between clear-sky 3D and IPA calculations, but this process is currently not automated.  
 752

Deleted: retrieval  
 Deleted: MYD09  
 Deleted: surface reflectance  
 Deleted: MYD09

Deleted: reflectance

Deleted: surface reflectance

753



754

755 **Figure 5.** (a) Latitudinally averaged (0.01° spacing) radiance calculations from EaR<sup>3</sup>T (red: 3D, blue: IPA) and OCO-  
 756 2 measured radiance at 768.52 nm (black) The green shaded area indicates the inset shown in (b). (b) The

763 same as Figure 2 except OCO-2 measured radiance overlaid on IPA radiance simulations at 768.52 nm. The  
764 solar zenith angle (SZA) for the radiance simulation case is 34.3°.

Deleted: 33.57

765  
766 In the cloudy locations (radiance value greater than ~0.05), the IPA calculations match the  
767 OCO-2 observations on a footprint-by-footprint level (see Figure 5b), demonstrating that wind and  
768 parallax corrections were performed successfully. Of course, there is not always a perfect  
769 agreement because of morphological changes in the cloud field over the course of six minutes. It  
770 is, however, apparent that the 3D calculations agree to a much lesser extent with the observations  
771 than the IPA calculations. Just like the mismatch for the clear-sky pixels indicates a bias in the  
772 input surface albedo, the bias here means that the input cloud properties (most importantly COT)  
773 are inaccurate. For most of the reflectance peaks, the 3D simulations are too low, which means  
774 that the input COT is biased low. This is due to 3D cloud effects on the MODIS-based cloud  
775 retrieval. Since they are done with IPA, any net horizontal photon transport is not considered,  
776 which leads to an apparent surface brightening as noted above, at the expense of the cloud  
777 brightness. As a result, the COT from darker clouds is significantly underestimated. This  
778 commonly known problem (Barker and Liu, 1995), with several aspects discussed in the  
779 subsequent EaR<sup>3</sup>T applications, can be identified by radiance consistency checks such as the one  
780 shown in Figure 5, and mitigated by novel types of cloud retrievals that do take horizontal photon  
781 transport into account (section 6).

Deleted: surface reflectance

#### 782 783 4.2 MODIS (App. 2)

784 To go beyond the OCO-2 track and understand the bias between simulated and observed  
785 radiances from a domain perspective, we now consider the radiance simulations for the MODIS  
786 650 nm channel. The setup is exactly the same as for the OCO-2 simulations, except that 1) the  
787 viewing zenith angle is set to the average viewing zenith angle of MODIS within the shown domain  
788 (instead of OCO-2), and 2) the surface albedo (or WSA) from MCD43 js used directly, this time  
789 from the 650 nm channel without rescaling. Figure 6a shows the MODIS measured radiance field,  
790 while Figure 6b shows the EaR<sup>3</sup>T 3D simulations. Visually, the clouds from the EaR<sup>3</sup>T simulation  
791 are generally darker than the observed clouds, which is in line with our aforementioned explanation  
792 of net horizontal photon transport. They are also blurrier because radiative smoothing (Marshak et  
793 al., 1995) propagates into the retrieved COT fields, which are subsequently used as input to EaR<sup>3</sup>T.

Deleted: surface reflectances

Deleted: MYD09

Deleted: are



799 The IPA RT calculations agree with the observations for clouds (see Figure A4a in Appendix C2),  
 800 which is expected as the IPA calculations and retrievals go through the same RT process, and the  
 801 darkening and smoothing effects (referred to as 3D effects) are due to horizontal photon transport.  
 802 To look at the 3D effects more quantitatively, Figure 7 shows a heatmap plot of simulated radiance  
 803 versus observed radiance. It shows that the radiance for cloud-covered pixels (labeled “cloudy”)  
 804 from EaR<sup>3</sup>T are mostly low-biased while good agreement between simulations and observations  
 805 was achieved for clear-sky radiance (labeled “clear-sky”). The good agreement over clear-sky  
 806 regions is expected. As mentioned above, we use MCD43 as surface albedo input, which in  
 807 contrast to the OCO-2 surface albedo product is appropriately cloud-screened and therefore does  
 808 not have a reflectance high bias. There is, of course, a reflectance enhancement in the vicinity of  
 809 clouds, but that is captured by the EaR<sup>3</sup>T calculations. The fact that the calculations agree with the  
 810 observations even for clear-sky pixels in the vicinity of clouds, shows that the concept of radiance  
 811 consistency works to ensure correct satellite retrievals even in the presence of clouds. It also  
 812 corroborates our observation from section 4.1 that COT<sub>IPA</sub> is low biased. Since the MODIS  
 813 reflectance is *not* self-consistent with respect to 3D RT calculations using COT<sub>IPA</sub> as shown for  
 814 the *cloudy* pixels in Figure 7, we can identify a bias in the cloud properties even without knowing  
 815 the ground truth of COT. On the other hand, successful closure in radiance (self-consistency)  
 816 would provide an indication that the input fields including COT are accurate, although it is  
 817 certainly a weaker metric than direct verification of the retrievals through aircraft-satellite retrieval  
 818 validation using observations from in-situ instruments.

Deleted: darkening and smoothing

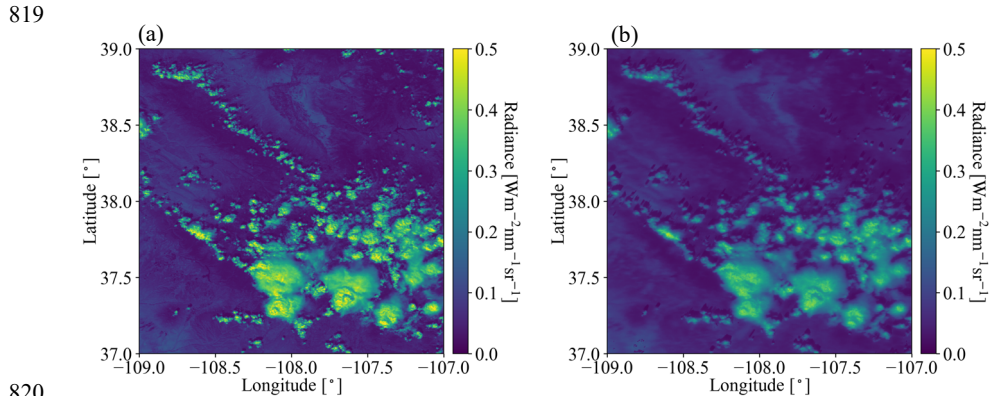
Deleted: MYD09

Deleted: surface reflectance

Deleted: surface reflectance

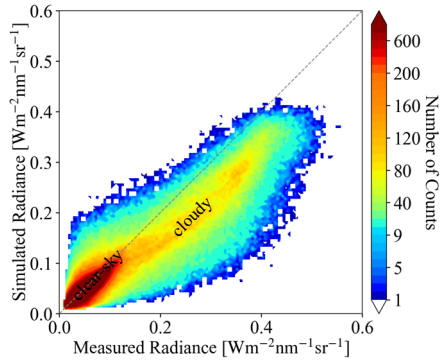
Deleted: aircraft

Deleted: with





827 **Figure 6. (a)** MODIS measured radiance in channel 1 (650 nm). **(b)** Simulated 3D radiance at 650 nm from EaR<sup>3</sup>T.  
 828 The solar zenith angle for the radiance simulation case is 34.94°.



831  
 832 **Figure 7.** Heatmap plot of EaR<sup>3</sup>T simulated 3D radiance vs. MODIS measured radiance at 650 nm.  
 833

834 Summarizing the two satellite radiance simulator applications, one can say that EaR<sup>3</sup>T  
 835 enables a radiance consistency check for inhomogeneous cloud scenes. We demonstrated that a  
 836 lack of simulation-observation consistency (MODIS versus OCO-2) and self-consistency (MODIS  
 837 versus MODIS) can be traced back to biased surface albedo or cloud fields in the simulator input.  
 838 This can become a diagnostic tool for the quality of retrieval products from future or current  
 839 missions, even when the ground truth is not known. Although not shown, the errors in the  
 840 simulated radiance associated with the fixed-SZA assumption (domain average) are negligible.  
 841 However, the vertical extent of the clouds affects the simulated radiance – the larger the vertical  
 842 extent, the larger the 3D effects (more horizontal photon transport). Since we make the assumption  
 843 of 1) a cloud geometric thickness of 1 km for clouds with CTH less than 4 km, and 2) cloud base  
 844 height of 3 km for clouds with CTH greater than 4km, the simulated radiance at the satellite sensor  
 845 level is valid for that proxy cloud only. For clouds that are geometrically thicker than the assumed  
 846 cloud geometrical thickness, the simulated radiance would be even lower due to enhanced  
 847 horizontal photon transport. Either way, the comparison with the actual radiance measurements  
 848 will reveal a lack of closure. Additionally, although the clouds introduce the lion's share of the 3D  
 849 bias that is identified by the radiance consistency check, additional discrepancies can be introduced

Deleted: 34.42

Deleted: surface reflectance

Deleted: It should be pointed out that

Deleted: if no thickness information is provided

Deleted: deeper

855 in different ways. For example, the topography (mountainous region in Colorado) is not considered  
856 by MCARaTS (it is considered by MYSTIC, but this solver has not been implemented yet).

857 For ~~the reference of simulation running time:~~ The MODIS simulation (domain size of  
858 [Nx=~~846~~, Ny=~~846~~]) took about ~~15 minutes~~, on a Linux workstation with ~~8~~ CPUs for three 3D RT  
859 runs with  $10^8$  photons. With a slightly modified setup and parallelization, the automation can be  
860 easily applied for entire satellite orbits, although more research is required to optimize the  
861 computation speed depending on the desired output accuracy.

862

### 863 5. EaR<sup>3</sup>T as 3D Aircraft Irradiance Simulator (App. 3)

864 In contrast to the previous applications that focused on satellite remote sensing, we will  
865 now be applying EaR<sup>3</sup>T to quantify 3D cloud retrieval biases through direct, systematic validation  
866 of imagery-derived *irradiances* against aircraft measurements, instead of using the indirect path  
867 of radiance consistency in section 4. Previous studies (e.g., Schmidt et al., 2007; Kindel et al.,  
868 2010) conducted radiative closure between remote sensing derived and measured irradiance using  
869 isolated flight legs as case studies. Here, with the efficiency afforded by the automated nature of  
870 EaR<sup>3</sup>T, we are able to conduct radiative closure of irradiance through a statistical approach that  
871 employs campaign-scale amounts of measurement data. Specifically, we used EaR<sup>3</sup>T to perform  
872 large-scale downwelling irradiance simulations at 745 nm based on geostationary cloud retrievals  
873 from AHI for the CAMP<sup>2</sup>Ex campaign, and directly compare these simulations to the SPN-S  
874 measured irradiances onboard the P-3 aircraft. This is done for all below-cloud legs from the entire  
875 campaign with the aim to assess the degree to which satellite-derived near-surface irradiances  
876 reproduce the true conditions below clouds.

877 The irradiance simulation process is similar to the previously described radiance simulation  
878 in section 4, with only a few modifications. First, we used cloud optical properties from the AHI  
879 cloud product (COT, CER and CTH) as direct inputs into EaR<sup>3</sup>T. Secondly, we used a constant  
880 ocean surface ~~albedo~~ value of 0.03. Such simplification in surface albedo is made under the  
881 assumption that 1) the ocean surface is calm with no whitecaps, and that 2) the Lambertian ~~BRDF~~  
882 is sufficient (instead of directionally dependent BRDF) to represent surface albedo for the  
883 irradiance calculation. Since the ocean surface albedo can greatly differ from 0.03 when the Sun  
884 is extremely low (Li et al., 2006), we excluded data under low-Sun conditions where the SZA is  
885 greater than 45°. Lastly, since EaR<sup>3</sup>T can only perform 3D simulations for a domain at a single

Deleted: technical

Deleted: 1188

Deleted: 1188

Deleted: one

Deleted: hour

Deleted: 12

Deleted: each

Deleted: reflectance

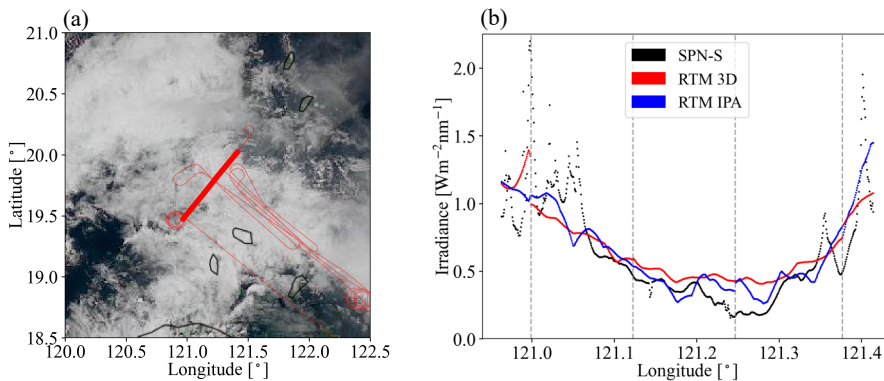
Deleted: bidirectional reflectance distribution function (BRDF)...

896 specified solar geometry, we divided each CAMP<sup>2</sup>Ex research flight into small flight track  
897 segments where each segment contains 6 minutes of flight time. The size and shape of the flight  
898 track segments can vary significantly due to the aircraft maneuvers, aircraft direction, aircraft  
899 speed, etc. For each flight track segment, EaR<sup>3</sup>T performs irradiance simulations for a domain that  
900 extends half a degree at an averaged solar zenith angle. In contrast to the radiance simulation output,  
901 which is two-dimensional at a specified altitude and sensor geometry, the irradiance simulation  
902 output is three dimensional. In addition to x (longitude) and y (latitude) vectors, it has a vertical  
903 dimension along z (altitude). From the simulated three-dimensional irradiance field, the irradiance  
904 for the flight track segment is linearly interpolated to the x-y-z location (longitude, latitude, and  
905 altitude) of the aircraft. EaR<sup>3</sup>T automatically sub-divides the flight track into tiles encompassing  
906 track segments, and extracts the necessary information from the aircraft navigational data. Based  
907 on the aircraft time and position, EaR<sup>3</sup>T downloads the AHI cloud product that is closest in time  
908 and space to the domain containing the flight track segment.

909 Figure 8 shows the simulated irradiance for a sample flight track below clouds on 20  
910 September, 2019. Figure 8a shows the flight track overlaid on AHI imagery. Figure 8b shows 3D  
911 (in red) and IPA (in blue) downwelling irradiance simulations for the highlighted flight track in  
912 Figure 8a, as well as measurements by the SPN-S (in black). Since the 3D and IPA simulations  
913 are performed separately at discrete solar and sensor geometries for each flight track segment based  
914 on potentially changing cloud fields from one geostationary satellite image to the next,  
915 discontinuities in the calculations (indicated by gray dashed lines) are expected. The diffuse  
916 irradiance (downwelling and upwelling) can also be simulated and compared with radiometer  
917 measurements (not shown here). Since the irradiance was simulated/measured below clouds, high  
918 values of downwelling irradiance indicate thin-cloud or cloud-free regions while low values of  
919 downwelling irradiance indicate thick-cloud regions. The simulations successfully captured this  
920 general behavior – clouds thickened from west to east until around 121.25° E, and thinned  
921 eastwards. However, the fine-scale variabilities in irradiance were not captured by the simulations  
922 due to the coarse resolution of COT in the AHI cloud product (3-5 km). Additionally, the  
923 simulations also missed the clear-sky regions in the very east and west of the flight track as  
924 indicated by high downwelling irradiance values measured by SPN-S. This is probably also due to  
925 the coarse resolution of the AHI COT product where small cloud gaps are not represented. Large  
926 discrepancies between simulations and observations occur in the mid-section of the flight track

927 where clouds are present (e.g., longitude range from 121.15° to 121.3°). Although the 3D  
 928 calculations differ somewhat from the IPA results, they are both biased high, likely because the  
 929 input COT (the IPA-retrieved AHI product) is biased low. This bias is caused by the same  
 930 mechanism that was discussed earlier in the MODIS examples (section 4.2). This begs the question  
 931 whether this is true for the entire field mission. To answer the question, we performed a *systematic*  
 932 comparison of the cloud transmittance for *all* available below-cloud flight tracks from CAMP<sup>2</sup>Ex,  
 933 using EaR<sup>3</sup>T's automated processing pipeline. The output of this pipeline is visualized in time-  
 934 synchronized flight videos (Chen et al., 2022), which show the simulations and observations along  
 935 all flight legs point by point. These videos give a glimpse of the general cloud environment during  
 936 the field campaign from the geostationary satellite perspective.

937  
 938

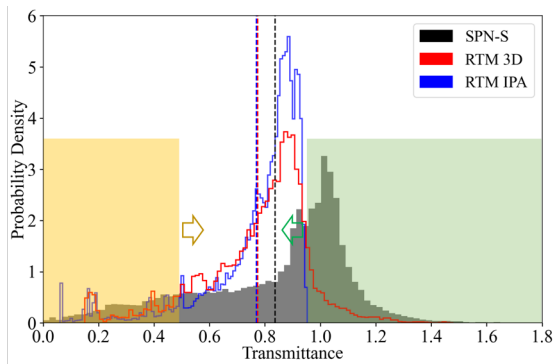


939 **Figure 8.** (a) Flight track overlay HIMAWARI AHI RGB imagery over the Philippine Sea on 20 September, 2019.  
 940 The thin line shows the entire flight track within the domain. The thick line highlights the specific leg  
 941 analyzed in (b). (b) Measured downwelling irradiance from SPN-S at 745 nm and calculated 3D and IPA  
 942 irradiance from EaR<sup>3</sup>T for the highlighted flight track in (a).  
 943  
 944

945 For this comparison, we use transmittance instead of irradiance. The transmittance is  
 946 calculated by dividing the downwelling irradiance below clouds ( $F_{\downarrow}^{bottom}$ ) by the downwelling  
 947 irradiance at the top of the atmosphere extracted from the Kurucz solar spectra ( $F_{\downarrow}^{TOA}$ ; Kurucz,  
 948 1992) at incident solar zenith angle (SZA), where

949 
$$Transmittance = \frac{F_{\downarrow}^{bottom}}{F_{\downarrow}^{TOA} \cdot \cos(SZA)}$$

950 Thus the transmittance has less diurnal dependence than the irradiance. Figure 9 shows the  
 951 histograms of the simulated and measured cloud transmittance from all below-cloud legs. The  
 952 average values are indicated by dashed lines. Although the averaged values of IPA and 3D  
 953 transmittance are close, their distributions are different. Only the 3D calculations and the measured  
 954 transmittance reach values beyond 1. This occurs in clear-sky regions in the vicinity of clouds that  
 955 receive photons scattered by the clouds as previously discussed for the OCO-2 application.  
 956



957  
 958 **Figure 9.** Histogram of measured transmittance from SPN-S at 745 nm (dark gray filled) and calculated 3D (red solid  
 959 line) and IPA (blue solid line) transmittance from EARTH3T for all the below-cloud flight tracks during  
 960 CAMP<sup>2</sup>Ex in 2019. The mean values are indicated by dashed lines. The yellow (green) shaded area  
 961 represents the relatively low (high) transmittance region where the probability density of the observed  
 962 transmittance (dark gray filled) is greater than the calculations.  
 963

964 Both the distribution and the mean value of the simulations are different from the  
 965 observations – the simulation histograms peak at around 0.9 while the observation histogram peaks  
 966 at around 1. The histograms indicate that the RT simulations miss most of the clear-sky conditions  
 967 because of the coarse resolution of the AHI cloud product. If clouds underfill a pixel, AHI  
 968 interprets the pixel as cloudy in most cases. This leads to an underestimation of clear-sky regions  
 969 since cumulus and high cirrus were ubiquitous during CAMP<sup>2</sup>Ex. The area on the left (highlighted  
 970 in yellow) has low cloud transmittance associated with thick clouds. In this range, the histograms  
 971 of the calculations are generally below the observations, and the PDF of the calculations is offset

Deleted: black

Deleted: black

974 to the right (indicated by the yellow arrow). This means that the transmittance is overestimated by  
975 both IPA and 3D RT, and thus that the COT of thick clouds is underestimated, consistent with  
976 what we found before (Figure 8b). The high-biased transmittance below-cloud is also consistent  
977 with the findings of low-biased reflectance (App. 1 and 2), both indicating COT of the optically  
978 thick clouds are low-biased. The high-transmittance end (highlighted in green) is associated with  
979 clear-sky and thin clouds. Here, the peak of the PDF is shifted to the left (green arrow), and the  
980 calculations are biased low. This is caused by a combination of 1) the overestimation in COT of  
981 thin clouds due a 3D bias in the AHI IPA retrieval, 2) the aforementioned resolution effect that  
982 underestimates the occurrence of clear-sky regions (or overestimation in cloud fraction), and 3)  
983 net horizontal photon transport from clouds into clear-sky pixels. Overall, the calculations  
984 underestimate the true transmittance by 10%. This might seem to contradict Figure 7, where the  
985 calculated reflected radiance was biased low due to the *underestimation* of COT in the heritage  
986 retrievals, which would correspond to an *overestimation* of the radiation transmitted by clouds.  
987 This effect is indeed apparent in the yellow-shaded area of Figure 9 (high COTs), but the means  
988 (dashed lines) show exactly the opposite. To understand that, one has to consider that the histogram  
989 depicts all-sky conditions, which include both cloudy and clear pixels. In this case, the direction  
990 of the overall (all-sky) bias follows the direction of the thin-cloud/clear bias, rather than the  
991 direction of the thick cloud bias. For different study regions of the globe with different cloud  
992 fractions, cloud size distributions, and possibly different imager resolutions, the direction and  
993 magnitude of the bias might be very different.

994 Summarizing, this application demonstrates that the EaR<sup>3</sup>T's automation feature allows  
995 systematic simulation-to-observation comparisons. If aircraft observations are available, then  
996 closure between satellite-derived irradiance and suborbital measurements is a more powerful  
997 verification of satellite cloud retrieval products than the radiance consistency from the earlier  
998 stand-alone satellite applications. Even more powerful is the new approach to process the data  
999 from an entire field mission for assessing the quality of cloud products in a region of interest (in  
1000 this case, the CAMP<sup>2</sup>Ex area of operation).

1001

## 1002 **6. EaR<sup>3</sup>T for Mitigating 3D Cloud Retrieval Biases (App. 4)**

1003 In this section, we will use high-resolution imagery from a radiometrically calibrated  
1004 all-sky camera flown during the CAMP<sup>2</sup>Ex to isolate the 3D bias (sometimes referred to as IPA

1005 bias) and explore its mitigation with a newly developed CNN cloud retrieval framework (Nataraja  
1006 et al., 2022). The CNN, unlike IPA, takes pixel-to-pixel net horizontal photon transport into  
1007 account. It exploits the spatial context of pixels in cloud radiance imagery, and extracts a higher-  
1008 dimensional, multi-scale representation of the radiance to retrieve COT fields as the output. It does  
1009 so by learning on “training data”, which in this case was input radiance and COT pairs synthetically  
1010 generated by EaR<sup>3</sup>T using LES data from the Sulu Sea. The best CNN model, trained on different  
1011 coarsened resolutions of the data pairs, is included within the EaR<sup>3</sup>T repository. For App. 4, this  
1012 CNN is applied to real imagery data for the first time, which in our case are near-nadir observations  
1013 by the all-sky camera (section 2.2.5) that flew in CAMP<sup>2</sup>Ex.

1014 The CNN model was trained at a single (fixed) sun-sensor geometry (solar zenith angle,  
1015 SZA=29.2°; solar azimuth angle, SAA=323.8°, viewing zenith angle, VZA=0°), at a spatial  
1016 resolution of 100 m. We therefore chose a camera scene with a matching SZA (28.9°), and rotated  
1017 the radiance imagery to match SAA=323.8°, and subsequently gridded the 8-12 m native  
1018 resolution camera data to 100 m. Figure 10a shows the RGB imagery captured by the all-sky  
1019 camera over the Philippine Sea at 02:10:06 UTC on 5 October 2019. The Sun is located at the  
1020 southeast (as indicated by the yellow arrow) and can be easily identified from the sun glint. Note  
1021 that this image has not yet been geolocated; it is depicted as acquired in the aircraft reference frame.  
1022 Figure 10b shows the rotated scene of the red channel radiance for the region encircled in yellow  
1023 in Figure 10a. The sun (as indicated by the yellow arrow) is now at SAA=323.8°. The selected  
1024 study region is indicated by the red rectangle in Figure 10b (6.4x6.4 km<sup>2</sup>), where the raw radiance  
1025 of the camera is gridded at 100 m resolution to match the spatial resolution of the training dataset  
1026 of the CNN.

1027  
1028

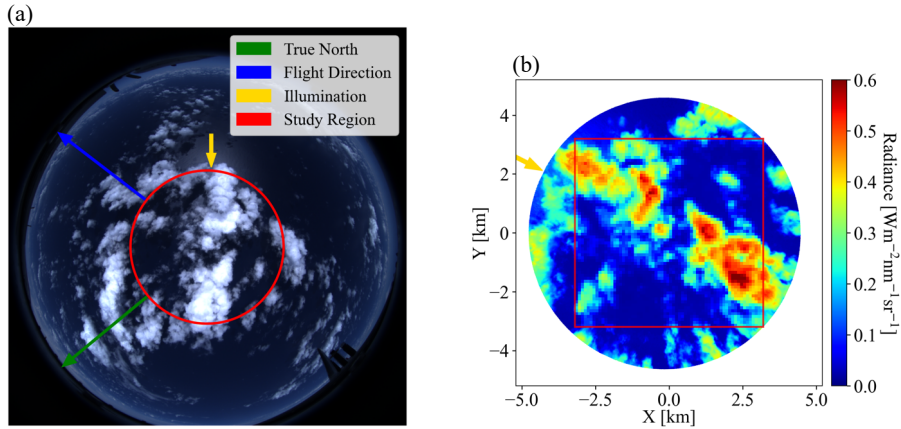


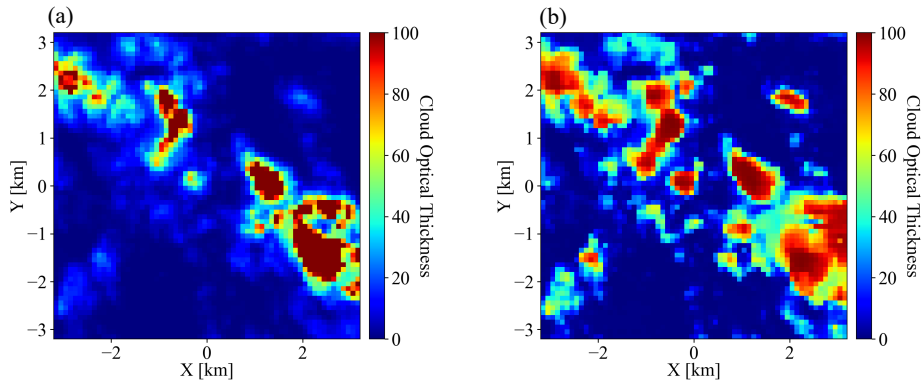
**Figure 10.** (a) RGB imagery of nadir-viewing all-sky camera deployed during CAMP<sup>2</sup>Ex for a cloud scene centered at [123.392°E, 15.2744°N] over the Philippine Sea at 02:10:06 UTC on 5 October, 2019. The arrows indicate the true north (green), flight direction (blue), and illumination (where the sunlight comes from, yellow). (b) Red channel radiance measured by the camera for the circular area indicated by the red circle in (a). Red squared region shows gridded radiance with a pixel size of 64x64 and spatial resolution of 100 m.

From the radiance field, we used both the traditional IPA (based on the [IPA reflectance-to-COT mapping](#)) and the new CNN to retrieve COT fields. Figure 11 shows the COT<sub>IPA</sub> and COT<sub>CNN</sub> fields, which are visually quite different. For relatively thin clouds (e.g., at around {2, 1.8}), the CNN tends to retrieve larger COT values than COT<sub>IPA</sub>. Also, it returns more spatial structure than the IPA (e.g., around {2,-1}). To assess how either retrieval performs, we now apply the radiance self-consistency approach introduced with MODIS data in section 4.2. Using both the IPA and the CNN retrieval as input, we had EaR<sup>3</sup>T calculate the (synthetic) radiance that the camera should have observed if the retrieval were accurate. The clouds are assumed to be located at 1-2 km. Such an assumption is inferred from low-level aircraft observations of clouds on the same day. These radiance fields are shown in Figure 12a and 12b, and can be compared to Figure 12c. Seven edge pixels have been removed from the original domain because the CNN performs poorly at edge pixels, and because the 3D calculations use periodic boundary conditions.

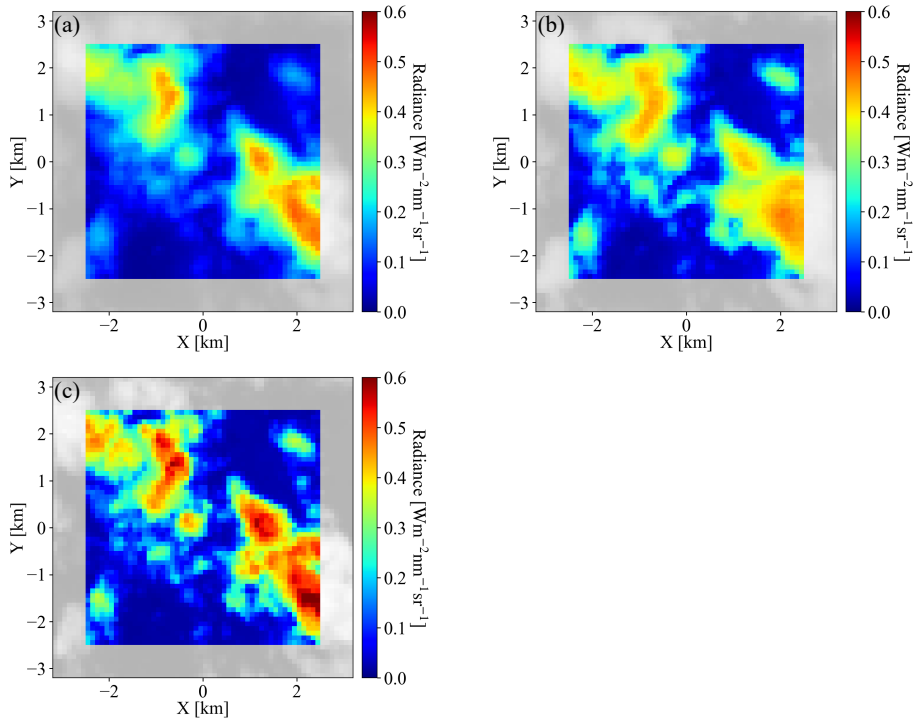
Deleted: two-stream

Deleted: approximation





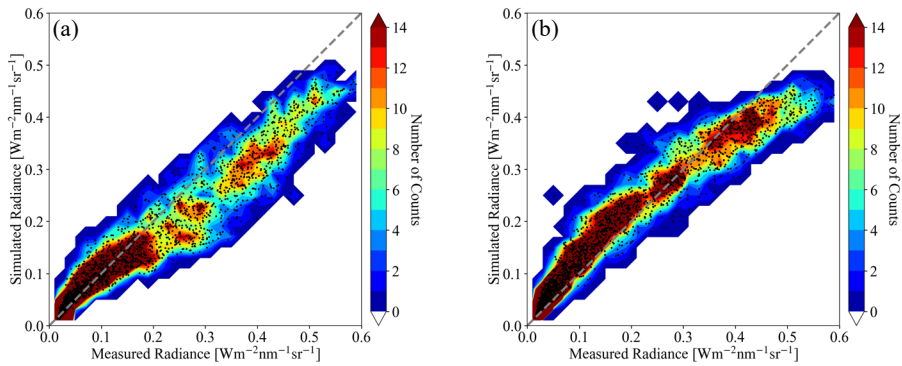
1052  
 1053 **Figure 11.** Cloud optical thickness for the gridded radiance in Figure 10b (a) estimated by IPA [method](#) and (b)  
 1054 predicted by CNN.  
 1055  
 1056



1057

1058

1059 **Figure 12.** 3D radiance calculations from EaR<sup>3</sup>T at 600 nm based on cloud optical thickness field **(a)** estimated by  
 1060 IPA, and **(b)** predicted by the CNN. The radiance measured by the all-sky camera (the same as Figure  
 1061 10b) is provided in the same format at **(c)** for comparison. The calculations were originally performed  
 1062 for the 64x64 domain. Then 7 pixels along each side of the domain (contoured in gray) were excluded,  
 1063 which resulted in a 50x50 domain.  
 1064  
 1065



1066 **Figure 13.** Scatter plot overlays 2D histogram of 3D radiance calculations at 600 nm based on cloud optical thickness  
 1067 **(a)** estimated by IPA and **(b)** predicted by the CNN vs. measured red channel radiance from all-sky camera.  
 1068  
 1069

1070 As evident from the brightest pixels in Figures 12b and 12c, the radiances simulated on the  
 1071 basis of the  $COT_{CNN}$  input are markedly lower than actually observed by the camera. This is  
 1072 because the CNN was trained on a LES dataset with limited COT range that excluded the largest  
 1073 COT that occurred in practice. This means that the observational data went beyond the original  
 1074 training envelope of the CNN, which highlights the importance of choosing the CNN training data  
 1075 carefully for a given region. In Figure 13, the simulations are directly compared with the original  
 1076 observations, confirming that indeed the CNN-generated data are below the observations on the  
 1077 high radiance end. Otherwise, the CNN-generated radiances agree with the observations. In  
 1078 contrast, the IPA-generated data are high biased for the optically very thin clouds (radiance below  
 1079 0.1) and systematically low-biased for the thick clouds (radiance above 0.2) when comparing with  
 1080 the observations, over the dynamic range of the COT, which is indicative of the 3D retrieval bias  
 1081 that we discussed earlier. A small high bias occurs in the  $COT_{CNN}$  based radiance simulations for  
 1082 the optically thin clouds (radiance value below 0.2). This probably because the CNN training as

Deleted: CNN COT

Deleted: lower

Deleted: than

1086 described by Nataraja et al. (2022) is 1) based on a surface albedo of 0 and 2) aerosol-free  
1087 atmospheric environment (also aerosol-free setup for radiance simulations in Figure 13), where in  
1088 reality the ocean is slightly brighter and atmosphere is mixed with aerosols. Here again, the  
1089 radiance self-consistency approach proves useful despite the absence of ground truth data for the  
1090 COT. This is valuable because in reality satellite remote sensing does not have the ground truth of  
1091 COT, whereas radiance measurements are always available. For the CNN, the self-consistency of  
1092 the radiance is remarkable for most of the clouds (radiance smaller than 0.4), which encompass  
1093 86.8% of the total number of image pixels.

1094 Finally, we use EaR<sup>3</sup>T to propagate the 3D cloud retrieval bias into the associated bias in  
1095 estimating the cloud radiative effect from passive imagery retrievals, which means that we are  
1096 returning from a remote sensing to an energy perspective (irradiance) at the end of the paper. The  
1097 calculated cloud radiative effects (CRE) of both below-clouds (at the surface) and above-clouds  
1098 (at 2.5 km) are shown in Figure 14a and 14b. The most important histograms are those from 3D  
1099 irradiance calculations based on the CNN retrievals (gray solid line), as this combination would  
1100 be used in a next-generation framework for deriving CRE from passive remote sensing, and the  
1101 other would be IPA irradiance calculations based on the IPA retrieval (red solid line), as done in  
1102 the traditional (heritage) approach. The dashed lines are the other combinations. The mean values  
1103 (red vs. gray) indicate that in our case the traditional approach would lead to a high bias of more  
1104 than to 28% both at the surface and 20% above clouds due to low-biased COT<sub>IPA</sub> (consistent with  
1105 findings of low-biased COT<sub>IPA</sub>-derived reflectance from App. 1&2 and high-biased COT<sub>IPA</sub>-  
1106 derived transmittance from App. 3). Here again, 3D biases do not cancel each other out in the  
1107 domain average. If the CNN had better fidelity even for optically thick clouds, the real bias in CRE  
1108 would be even larger. A minor, but interesting finding is that regardless of which COT retrieval is  
1109 used, the mean CRE is similar for IPA and 3D irradiance calculations (e.g.,  $\overline{CRE_{IPA}(COT_{CNN})} \approx$   
1110  $\overline{CRE_{3D}(COT_{CNN})}$ , blue vertical dashed line locates near to gray vertical solid line), even though  
1111 the PDFs are different. By far the largest impact on accuracy comes from the retrieval technique,  
1112 not from the subsequent CRE calculations. Here again, the self-consistency check turns out as a  
1113 powerful metric to assess retrieval accuracy. Of course, we only used a single case in this part of  
1114 the paper. For future evaluation of the CNN versus the IPA, one would need to process larger  
1115 quantities of data in an automated fashion as done in the first part of the paper. This is beyond the  
1116 scope of this introductory paper, and will be included in future releases of EaR<sup>3</sup>T and the CNN.

Deleted: extremely helpful

Deleted: the thinner

Deleted: 83.5

Deleted: 3

Deleted: 25

Deleted:

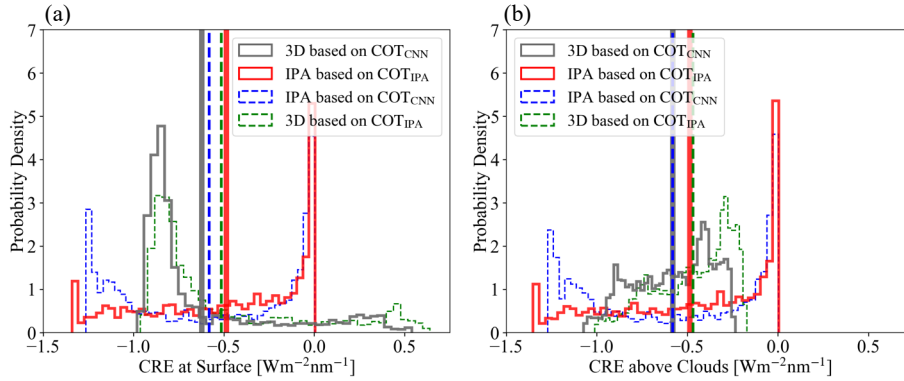
Deleted: very

Deleted: overlay

Deleted: very

Deleted: dissimilar

1127



1128

1129

1130

1131

1132

1133

1134

## 7. Summary and Conclusion

1135

1136

1137

1138

1139

1140

1141

1142

1143

1144

1145

1146

1147

1148

1149

In this paper, we introduced EaR<sup>3</sup>T, a toolbox that provides high-level interfaces to automate and facilitate 1D- and 3D-RT calculations. We presented applications that used EaR<sup>3</sup>T to:

- a) build a processing pipeline that can automatically simulate 3D radiance fields for satellite instruments (currently OCO-2 and MODIS) from publicly available satellite surface and cloud products at any given time over any specific region;
- b) build a processing pipeline that can automatically simulate irradiance along all flight legs of aircraft missions, based on geostationary cloud products;
- c) simulate radiance and irradiance for high-resolution COT fields retrieved from an airborne camera, using both a traditional 1D-RT (IPA) approach, and a newly developed 3D-RT (CNN) approach that considers the spatial context of a pixel.

Unlike other satellite simulators that employ 1D-RT, EaR<sup>3</sup>T is capable of performing the radiance and irradiance calculations in 3D-RT mode. Optionally, it can be turned off to link back to traditional 1D-RT codes, and to calculate 3D perturbations by considering the changes of 3D-RT fields relative to the 1D-RT baseline.

1150 With the processing pipeline under a) (App. 1 and App. 2, section 4), we prototyped a  
1151 3D-RT powered radiance loop (we call it “radiance self-consistency”) that is envisioned for  
1152 upcoming satellite missions such as EarthCARE and AOS. Retrieved cloud fields (in our case,  
1153 from MODIS and from an airborne camera) are fed back into a 3D-RT simulation engine to  
1154 calculate at-sensor radiances, which are then compared with the original measurements. Beyond  
1155 currently included sensors, others can be added easily, taking advantage of the modular design of  
1156 EaR<sup>3</sup>T. This radiance closure loop facilitates the evaluation of passive imagery products,  
1157 especially under spatially inhomogeneous cloud conditions. The automation of EaR<sup>3</sup>T permits  
1158 calculations at any time and over any given region, and statistics can be built by looping over entire  
1159 orbits as necessary. The concept of radiance self-consistency could be valuable even for existing  
1160 imagery datasets because it allows the automated quantification of 3D-RT biases even without  
1161 ground truth such as airborne irradiance from suborbital activities. Also, it can be easily extended  
1162 to spectral or multi-angle observations as available from MODIS and MISR (Multi-Angle Imaging  
1163 Spectroradiometer), and thus providing more powerful constraints to the remote sensing products.  
1164 In the future it should be possible to include a 3D-RT pipeline such as EaR<sup>3</sup>T into operational  
1165 processing of satellite derived data products.

Deleted: consistency

1166 Benefitting from the automation of EaR<sup>3</sup>T in b) (App. 3, section 5), we performed 3D-RT  
1167 irradiance calculations for the entire CAMP<sup>2</sup>Ex field campaign, moving well beyond radiation  
1168 closure case studies, and instead systematically evaluating satellite-derived radiation fields with  
1169 aircraft data for an entire region. From the comparison based on all below-cloud flight tracks  
1170 during the entire campaign, we found that the satellite-derived cloud transmittance was biased low  
1171 by 10% compared to the observations when relying on the heritage satellite cloud product.

1172 From the statistical results of the CAMP<sup>2</sup>Ex irradiance closure in b), we concluded that the  
1173 bias between satellite-derived irradiances and the ground truth from aircraft measurements was  
1174 due to a combination of the coarse spatial resolution of the geostationary imagery products and  
1175 3D-RT effects. To minimize the coarse-resolution part of the bias and thus to isolate the 3D-RT  
1176 bias, we used high-resolution airborne camera imagery in c) (App. 4, section 6), and found that  
1177 even with increased imager resolution, biases persisted. The at-sensor radiance derived from  
1178 COT<sub>IPA</sub> was inconsistent with the original measurements. For cloudy pixels, the calculated  
1179 radiance was well below the observations, confirming an overall low bias in COT<sub>IPA</sub>. This low bias  
1180 could be largely mitigated with the context-aware CNN developed separately in Nataraja et al.

Deleted: IPA COT retrievals

Deleted: IPA COT

1184 (2022) and included in EaR<sup>3</sup>T. Of course, this novel technique has limitations. For example, the  
1185 camera reflectance data went beyond the CNN training envelope, which would need to be extended  
1186 to larger COT in the future. In addition, the CNN only reproduces two-dimensional clouds fields  
1187 and does not provide access to the vertical dimension, which will be the next frontier to tackle.  
1188 Still, the greatly improved radiance consistency from COT<sub>IPA</sub> to COT<sub>CNN</sub> indicates that the EaR<sup>3</sup>T-  
1189 LES-CNN approach shows great promise for the mitigation of 3D-RT biases associated with  
1190 heritage cloud retrievals. We also discovered that for this particular case, the CRE calculated from  
1191 traditional 1D cloud products can introduce a warm bias of at least 28% at the surface and 20%  
1192 above clouds.

Deleted: 25

1193 EaR<sup>3</sup>T has proven to be capable of facilitating 3D-RT calculations for both remote sensing  
1194 and radiative energy studies. Beyond the applications described in this paper, EaR<sup>3</sup>T has already  
1195 been extensively used by a series of on-going research projects such as producing massive 3D-RT  
1196 calculations as training data for a new generation of CNN models (Nataraja et al., 2022), evaluating  
1197 3D cloud radiative effects associated with aerosols (Gristey et al., 2022), creating flight track and  
1198 satellite track simulations for mission planning etc. More importantly, the strategies provided in  
1199 this paper put novel machine learning algorithms on a physical footing, opening the door for the  
1200 mitigation of complexity-induced biases in the near-future. More development effort will be  
1201 invested into EaR<sup>3</sup>T in the future, with the goals of minimizing the barriers to using 3D-RT  
1202 calculations, and to promote 3D cloud studies. EaR<sup>3</sup>T will continue to be an educational tool driven  
1203 by graduate students. In the future, we plan to add support for additional publicly available 3D RT  
1204 solvers, e.g., SHDOM (Spherical Harmonic Discrete Ordinate Method, Evans, 1998; Pincus and  
1205 Evans, 2009), as well as built-in support for HITRAN and associated correlated-k methods  
1206 (currently, we are implementing such an approach for the longwave wavelength range). From a  
1207 research perspective, we anticipate that EaR<sup>3</sup>T will enable the systematic quantification and  
1208 mitigation of 3D-RT biases of imagery-derived cloud-aerosol radiative effects, and may be the  
1209 starting point for operational use of 3D-RT for future satellite missions.

Moved (insertion) [1]

Deleted: In addition to MCARaTS, planned solvers for the future include MYSTIC (Monte Carlo code for the physically correct tracing of photons in cloudy atmospheres, Mayer, 2009) and

Deleted: , e.g., SHDOM

1210

1217 **Appendix A**

1218 **A1 - Technical Input and Output Parameters of EaR<sup>3</sup>T**

1219 EaR<sup>3</sup>T provides various functions that can be combined to tailored pipelines for automatic  
1220 3D radiative transfer (3D-RT) calculations as described [in this paper](#) (App. 1 – 5), as well as for  
1221 complex research projects beyond. Since EaR<sup>3</sup>T is written in Python, the modules and functions  
1222 can be integrated into existing functions developed by the users themselves. Parallelization is  
1223 enabled in EaR<sup>3</sup>T by default through multi-processing to accelerate computations. If multiple  
1224 CPUs are available, EaR<sup>3</sup>T will distribute jobs for the 3D RT calculations. By default, the  
1225 maximum number of CPUs will be used. Since EaR<sup>3</sup>T is designed to make the process of setting  
1226 up and running 3D-RT calculations simple, some parameters that are unavailable from the input  
1227 data but are required by the RT solvers are populated via default values and assumptions. However,  
1228 this does not mean that by using EaR<sup>3</sup>T, one must use these assumptions; they can be easily  
1229 superseded by user-provided settings. To facilitate this process, Table A1 provides a detailed list  
1230 of parameters (subject to change in future updates) that can be controlled and modified by the user.  
1231 In `examples/02_modis_rad-sim.py`, we defined these user-controllable parameters as  
1232 global variables for providing easy access to user. In the future, most of the parameters will be  
1233 controllable through a dedicated configuration file for optimal transparency. These parameters can  
1234 be changed within the code. For instance, by changing the parameters of `'date'` (Line 67 in  
1235 `examples/02_modis_rad-sim.py`) and `'region'` (Line 68 in  
1236 `examples/02_modis_rad-sim.py`) [within params](#) into the following:

1237 `params['date'] = datetime.datetime(2022, 2, 10)`

1238 `params['region'] = [-6.8, -2.8, 17.0, 21.0]`

1239 one can perform similar RT calculations (as demonstrated in App. 2) for another date and region  
1240 of interest (here, west Sahara Desert on 10 February, 2022). [Note that the code is under active  
1241 development, the line numbers are only valid in the version release of v0.1.1 and might change in  
1242 the future. Given the input parameters, EaR<sup>3</sup>T will calculate radiance or irradiance and save the  
1243 calculations into a HDF5 \(Hierarchical Data Format version 5\) file. The output data variables are  
1244 provided in Table A2.](#)

1245 In addition [to the example code](#), intuitive and simple examples are provided in  
1246 `examples/00_er3t_mca.py` and `examples/00_er3t_lrt.py` for users who are  
1247 interested in learning the basics of setting up EaR<sup>3</sup>T for calculations. At the current stage, only

Deleted: App. 1 – 5 of

Deleted: \_date

Deleted: \_region

Deleted: \_date

Deleted: \_region

Deleted: Note that the cloud detection algorithms we included in the code are imperfect (they only work satisfactorily for the App. 2 case we presented in this paper); for other regions on the globe, they may need to be adjusted.

Deleted: Automation of this feature is planned for the future

1258 limited documentation is provided. However, community support is available from the author of  
 1259 this paper through Discord<sup>6</sup>. In the near-future, more effort will be invested into documentation to  
 1260 give the user more autonomy in creating new applications that cannot be derived from those  
 1261 provided in our paper.  
 1262

| Parameters                          | App. 1   | App. 2  | App. 3  | App. 4  | App. 5   |
|-------------------------------------|--|---|---|---|--|
|                                     | examples/01_oc<br>o2_rad-sim.py  | examples/02_mo<br>dis_rad-sim.py  | examples/03_sp<br>ns_flux-sim.py  | examples/04_ca<br>m_nadir_rad-<br>sim.py  | examples/05_cn<br>n-les_rad-<br>sim.py   |
| Date                                | September 2, 2019<br>Specified at Line 66:<br><a href="#">params['date']</a><br>And Line 1569:<br><a href="#">date</a>   | September 2, 2019<br>Specified at Line 68:<br><a href="#">params['date']</a><br>And Line 1311:<br><a href="#">date</a>  | September 20, 2019<br>Specified at Line 439:<br><a href="#">date</a><br>And Line 238:<br><a href="#">date</a>           | October 5, 2019<br>Specified at Line 59:<br><a href="#">params['date']</a><br>And Line 215:<br><a href="#">date</a>   | <a href="#">October 5, 2019</a><br>Specified at Line 58:<br><a href="#">params['date']</a><br>And Line 126:<br><a href="#">date</a>      |
| Geographical Region                 | Specified at Line 69:<br><a href="#">params['region']</a>  | Specified at Line 69:<br><a href="#">params['region']</a>   | Variable (depends on aircraft location)   | N/A   | N/A  |
| Z Grid (Number of Grids/Resolution) | 40 / 0.5 km<br>Specified at Line 1476:<br><a href="#">levels</a>   | 40 / 0.5 km<br>Specified at Line 1220:<br><a href="#">levels</a>  | 20 / 1 km<br>Specified at Line 180:<br><a href="#">levels</a>   | 40 / 0.5 km<br>Specified at Line 174:<br><a href="#">levels</a>   | <a href="#">50 / 0.4km</a><br>Specified at Line 92:<br><a href="#">levels</a>  |
| Wavelength                          | <a href="#">768.52 nm</a><br>Specified at Line 67:<br><a href="#">params['wavelength']</a>   | 650 nm<br>Specified at Line 67:<br><a href="#">params['wavelength']</a>   | 745 nm<br>Specified at Line 440:<br><a href="#">wavelength</a>  | 600 nm<br>Specified at Line 58:<br><a href="#">params['wavelength']</a>   | 600 nm<br>Specified at Line 57:<br><a href="#">params['wavelength']</a>  |
| Atmospheric Gas Profile             | US standard atmosphere<br>Specified at Line 1479:<br><a href="#">atm0</a>  | US standard atmosphere<br>Specified at Line 1223:<br><a href="#">atm0</a>   | US standard atmosphere<br>Specified at Line 183:<br><a href="#">atm0</a>  | US standard atmosphere<br>Specified at Line 177:<br><a href="#">atm0</a>  | US standard atmosphere<br>Specified at Line 68:<br><a href="#">params['atmospheric profile']</a><br>And Line 94:<br><a href="#">atm0</a> |
| Atmospheric Gas Absorption          | Case specific<br>Specified at Line 1487:<br><a href="#">abs0</a>   | Default Absorption Database (Coddington et al., 2008)<br>Specified at Line 1230:<br><a href="#">abs0</a>  | Default Absorption Database (Coddington et al., 2008)<br>Specified at Line 189:<br><a href="#">abs0</a>                 | Default Absorption Database (Coddington et al., 2008)<br>Specified at Line 184:<br><a href="#">abs0</a>               | Default Absorption Database (Coddington et al., 2008)<br>Specified at Line 97:<br><a href="#">abs0</a>                                   |
| Cloud Top Height (CTH)              | From MODIS L2 cloud product<br>Specified at Line 1520:<br><a href="#">data['cth_2d']</a><br>And Line 1530:<br><a href="#">cld0</a>   | From MODIS L2 cloud product<br>Specified at Line 1263:<br><a href="#">data['cth_2d']</a><br>And Line 1273:<br><a href="#">cld0</a>                                | From AHI L2 cloud product<br>Specified at Line 208:<br><a href="#">cth_2d</a><br>And Lines 212:<br><a href="#">cld0</a> | 2 km<br>Specified at Line 63:<br><a href="#">params['cloud_top height']</a><br>And Lines 199:<br><a href="#">cld0</a> | From LES<br>Specified at Line 103:<br><a href="#">cld0</a>   |
| Cloud Geometrical Thickness         | <a href="#">1 km for CTH &lt; 4 km</a> ;<br><a href="#">Variable that cloud base height is at 3 km for CTH &gt; 4 km</a><br>Specified at Line 1527:<br><a href="#">cgt</a> | <a href="#">1 km for CTH &lt; 4 km</a> ;<br><a href="#">Variable that cloud base height is at 3 km for CTH &gt; 4 km</a><br>And Line 1270:<br><a href="#">cgt</a> | 1 km<br>Specified at Line 212:<br><a href="#">cgt</a>   | 1 km<br>Specified at Line 64:<br><a href="#">params['cloud geometrical thickness']</a>                                | From LES<br>Specified at Line 103:<br><a href="#">cld0</a>   |

<sup>6</sup> <https://discord.gg/ntqsguwaWv>



|                           |  |  |   |  |   |
|---------------------------|--|--|---|--|---|
| Cloud Optical Thickness   | Used IPA reflectance-to-COT mapping for MODIS LTB Reflectance at 250 m resolution<br>Specified at Line <a href="#">1518: data['cot_2d']</a><br>And Line <a href="#">1530: c1d0</a> | Used IPA reflectance-to-COT mapping for MODIS LTB Reflectance at 250 m resolution<br>Specified at Line <a href="#">1261: data['cot_2d']</a><br>And Line <a href="#">1273: c1d0</a> | From AHI L2 cloud product<br>Specified at Line <a href="#">198: cot_2d</a><br>And Lines <a href="#">212: c1d0</a> | Used IPA reflectance-to-COT mapping and CNN for camera red channel radiance/reflectance at 100 m resolution<br>Specified at Lines <a href="#">474 and 493: cot_2d</a><br>And Lines <a href="#">199: c1d0</a> | From LES<br>Specified at Line <a href="#">103: c1d0</a>   |
| Cloud Effective Radius    | From MODIS L2 Cloud Product<br>Specified at Line <a href="#">1519: data['cer_2d']</a><br>And Line <a href="#">1530: c1d0</a>   | From MODIS L2 Cloud Product<br>Specified at Line <a href="#">1262: data['cer_2d']</a><br>And Line <a href="#">1273: c1d0</a>   | From AHI L2 cloud product<br>Specified at Line <a href="#">199: cer_2d</a><br>And Lines <a href="#">212: c1d0</a> | 12 micron<br>Specified at Lines <a href="#">475 and 494: cer_2d</a><br>And Lines <a href="#">199: c1d0</a>   | From LES<br>Specified at Line <a href="#">103: c1d0</a>   |
| Scattering Phase Function | Mie (water cloud)<br>Specified at Line <a href="#">1536: pha0</a><br>And Line <a href="#">1573: sca</a>  | Mie (water cloud)<br>Specified at Line <a href="#">1279: pha0</a><br>And Line <a href="#">1315: sca</a>  | Mie (water cloud)<br>Specified at Line <a href="#">219: pha0</a><br>And Line <a href="#">237: sca</a>             | Mie (water cloud)<br>Specified at Line <a href="#">190: pha0</a><br>And Line <a href="#">219: sca</a>  | Mie (water cloud)<br>Specified at Line <a href="#">111: pha0</a><br>And Line <a href="#">130: sca</a>   |
| Surface Albedo            | From MODIS surface albedo product and scaled by OCO-2<br>Specified at Line <a href="#">1501: mod43</a><br>And Line <a href="#">1503: sfc_2d</a>                                    | From MODIS surface albedo product<br>Specified at Line <a href="#">1244: mod43</a><br>And Line <a href="#">1246: sfc_2d</a>  | 0.03<br>Implicitly specified by default at Line <a href="#">234: mcarats_ng</a>                                   | 0.03<br>Specified at <a href="#">Line 61: params['surface_albedo']</a><br>And Line <a href="#">218: surface_albedo</a>   | Specified at Line <a href="#">59: params['surface_albedo']</a><br>And Line <a href="#">133: surface_albedo</a>                                  |
| Solar Zenith Angle        | From OCO-2 geolocation file<br>Specified at Line <a href="#">1554: sza</a><br>And Line <a href="#">1576: solar_zenith_angle</a>  | From MODIS geolocation file<br>Specified at Line <a href="#">1296: sza</a><br>And Line <a href="#">1318: solar_zenith_angle</a>  | Variable (depends on aircraft location and date and time)   | 28.90°<br>Specified at Line <a href="#">464: geometry['sza']</a><br>And Line <a href="#">222: solar_zenith_angle</a>   | 29.16°<br>Specified at Line <a href="#">60: params['solar_zenith_angle']</a><br>And Line <a href="#">134: solar_zenith_angle</a>                |
| Solar Azimuth Angle       | From OCO-2 geolocation file<br>Specified at Line <a href="#">1555: saa</a><br>And Line <a href="#">1577: solar_azimuth_angle</a>   | From MODIS geolocation file<br>Specified at Line <a href="#">1297: saa</a><br>And Line <a href="#">1319: solar_azimuth_angle</a>   | Variable (depends on aircraft location and date and time)   | 296.83°<br>Specified at Line <a href="#">465: geometry['saa']</a><br>And Line <a href="#">223: solar_azimuth_angle</a>   | 296.83°<br>Specified at Line <a href="#">61: params['solar_azimuth_angle']</a><br>And Line <a href="#">135: solar_azimuth_angle</a>             |
| Sensor Altitude           | 705 km (satellite altitude)<br>Implicitly specified by default at Line <a href="#">1568: mcarats_ng</a>  | 705 km (satellite altitude)<br>Implicitly specified by default at Line <a href="#">1310: mcarats_ng</a>  | N/A, three-dimensional irradiance outputs at user-defined Z grid  | 5.48 km (flight altitude)<br>Specified at Line <a href="#">466: geometry['alt']</a><br>And Line <a href="#">224: sensor_altitude</a>   | 705 km (satellite altitude)<br>Specified at Line <a href="#">64: params['sensor_altitude']</a><br>And Line <a href="#">138: sensor_altitude</a> |
| Sensor Zenith Angle       | From OCO-2 geolocation file<br>Specified at Line <a href="#">1557: vza</a>   | From MODIS geolocation file<br>Specified at Line <a href="#">1302: vza</a>   | 0° (nadir)<br>Implicitly specified by default at Line <a href="#">234: mcarats_ng</a>                             | 0° (nadir)<br>Implicitly specified by default at Line <a href="#">214: mcarats_ng</a>  | 0° (nadir)<br>Specified at Line <a href="#">62: params['sensor_zenith_angle']</a>   |

|                      |  |  |  |  |  |
|----------------------|--|--|--|--|--|
|                      | And Line <a href="#">1578</a> :<br><b>sensor_zenith_angle</b>  | And Line <a href="#">1320</a> :<br><b>sensor_zenith_angle</b>  |  |  | And Line <a href="#">136</a> :<br><b>sensor_zenith_angle</b>   |
| Sensor Azimuth Angle | From OCO-2 geolocation file<br><br>Specified at Line <a href="#">1558</a> : <b>vaa</b><br>And Line <a href="#">1579</a> :<br><b>sensor_azimuth_angle</b> | From MODIS geolocation file<br><br>Specified at Line <a href="#">1303</a> : <b>vaa</b><br>And Line <a href="#">1321</a> :<br><b>sensor_azimuth_angle</b> | 0° (insignificant for nadir)<br><br>Implicitly specified by default at Line <a href="#">234</a> :<br><b>mcarats_ng</b>                                 | 0° (insignificant for nadir)<br><br>Implicitly specified by default at Line <a href="#">214</a> :<br><b>mcarats_ng</b>                                 | 0° (insignificant for nadir)<br><br>Specified at Line <a href="#">63</a> :<br><b>params['sensor_azimuth_angle']</b><br>And Line <a href="#">137</a> :<br><b>sensor_azimuth_angle</b> |
| Number of Photons    | 1×10 <sup>8</sup> per run<br><br>Specified at Line <a href="#">70</a> :<br><b>params['photon']</b><br>And Line <a href="#">1583</a> :<br><b>photons</b>  | 1×10 <sup>8</sup> per run<br><br>Specified at Line <a href="#">70</a> :<br><b>params['photon']</b><br>And Line <a href="#">1325</a> :<br><b>photons</b>  | 1×10 <sup>7</sup> per run<br><br>Specified at Line <a href="#">50</a> :<br><b>params['photon']</b><br>And Line <a href="#">243</a> :<br><b>photons</b> | 1×10 <sup>7</sup> per run<br><br>Specified at Line <a href="#">60</a> :<br><b>params['photon']</b><br>And Line <a href="#">228</a> :<br><b>photons</b> | 1×10 <sup>8</sup> per run<br><br>Specified at Line <a href="#">65</a> :<br><b>params['photon']</b><br>And Line <a href="#">141</a> :<br><b>photons</b>                               |
| Number of Runs       | 3<br><br>Specified at Line <a href="#">1581</a> : <b>Nrun</b>  | 3<br><br>Specified at Line <a href="#">1323</a> : <b>Nrun</b>  | 3<br><br>Specified at Line <a href="#">242</a> : <b>Nrun</b>   | 3<br><br>Specified at Line <a href="#">226</a> : <b>Nrun</b>   | 3<br><br>Specified at Line <a href="#">140</a> : <b>Nrun</b>   |
| Mode (3D or IPA)     | 3D and IPA<br><br>Specified at Line <a href="#">1704</a> and <a href="#">1705</a> :<br><b>solver</b><br>And Line <a href="#">1584</a> :<br><b>solver</b> | 3D or IPA<br><br>Specified at Line <a href="#">1418</a> : <b>solver</b><br>And Line <a href="#">1326</a> :<br><b>solver</b>                              | 3D and IPA<br><br>Specified at Lines <a href="#">377</a> and <a href="#">378</a> :<br><b>solver</b><br>And Line <a href="#">244</a> :<br><b>solver</b> | 3D<br><br>Specified at Lines <a href="#">507</a> and <a href="#">508</a> :<br><b>solver</b><br>And Line <a href="#">229</a> :<br><b>solver</b>         | 3D<br><br>Specified at Line <a href="#">143</a> : <b>solver</b>  |
| Parallelization Mode | Python multiprocessing<br><br>Specified at Line <a href="#">1586</a> : <b>mp_mode</b><br><a href="#">12</a>  | Python multiprocessing<br><br>Specified at Line <a href="#">1328</a> : <b>mp_mode</b><br><a href="#">12</a>  | Python multiprocessing<br><br>Specified at Line <a href="#">247</a> : <b>mp_mode</b><br><a href="#">12</a>   | Python multiprocessing<br><br>Specified at Line <a href="#">231</a> : <b>mp_mode</b><br><a href="#">12</a>   | Python multiprocessing<br><br>Specified at Line <a href="#">145</a> : <b>mp_mode</b><br><a href="#">12</a>   |
| Number of CPUs       | Specified at Line <a href="#">71</a> :<br><b>params['Ncpu']</b><br>And Line <a href="#">1585</a> :<br><b>Ncpu</b>  | Specified at Line <a href="#">71</a> :<br><b>params['Ncpu']</b><br>And Line <a href="#">1327</a> :<br><b>Ncpu</b>  | Specified at Line <a href="#">311</a> : <b>Ncpu</b><br>And Line <a href="#">246</a> : <b>Ncpu</b>  | Specified at Line <a href="#">230</a> : <b>Ncpu</b>  | 24 on clusters<br><br>Specified at Line <a href="#">144</a> : <b>Ncpu</b>  |

1263  
1264  
1265  
1266  
1267  
1268  
1269

**Table A1:** List of parameters used in the five applications. The line numbers used in the table are referring to the code script of each application. If two line numbers are provided, the first one indicates where the parameter is defined and the second one indicates where the parameter is passed into the radiative transfer setup. Users can change either one for customization purposes.

| Metadata      |                           |               |           |
|---------------|---------------------------|---------------|-----------|
| Variable Name | Description               | Data Type     | Dimension |
| mean/N_photon | Number of photons per run | Array         | N_g       |
| mean/N_run    | Number of runs            | Integer value | N/A       |
| mean/toa      | TOA downwelling flux      | Float value   | N/A       |
| Radiance      |                           |               |           |
| Variable Name | Description               | Data Type     | Dimension |

| mean/rad                | Radiance field at user specified altitude averaged over different runs       | Array     | (N <sub>x</sub> , N <sub>y</sub> )                  |
|-------------------------|--|-----------|---|
| mean/rad_std            | Standard deviation of the radiance fields from different runs                | Array     | (N <sub>x</sub> , N <sub>y</sub> )                  |
| <b>Irradiance</b>       |  |           |   |
| Variable Name           | Description  | Data Type | Dimension   |
| mean/f_down             | Downwelling irradiance averaged over different runs                          | Array     | (N <sub>x</sub> , N <sub>y</sub> , N <sub>z</sub> ) |
| mean/f_down_std         | Standard deviation of the downwelling irradiance from different runs         | Array     | (N <sub>x</sub> , N <sub>y</sub> , N <sub>z</sub> ) |
| mean/f_down_diffuse     | Diffuse downwelling irradiance averaged over different runs                  | Array     | (N <sub>x</sub> , N <sub>y</sub> , N <sub>z</sub> ) |
| mean/f_down_diffuse_std | Standard deviation of the diffuse downwelling irradiance from different runs | Array     | (N <sub>x</sub> , N <sub>y</sub> , N <sub>z</sub> ) |
| mean/f_down_direct      | Direct downwelling irradiance averaged over different runs                   | Array     | (N <sub>x</sub> , N <sub>y</sub> , N <sub>z</sub> ) |
| mean/f_down_direct_std  | Standard deviation of the direct downwelling irradiance from different runs  | Array     | (N <sub>x</sub> , N <sub>y</sub> , N <sub>z</sub> ) |
| mean/f_up               | Upwelling irradiance averaged over different runs                            | Array     | (N <sub>x</sub> , N <sub>y</sub> , N <sub>z</sub> ) |
| mean/f_up_std           | Standard deviation of the upwelling irradiance from different runs           | Array     | (N <sub>x</sub> , N <sub>y</sub> , N <sub>z</sub> ) |

1270

1271 **Table A2:** Data variables contained in the output HDF5 file from EaR<sup>3</sup>T for radiance and irradiance calculations. The  
 1272 radiance is simulated with a user-specified sensor geometry at a given altitude using forward photon tracing.  
 1273 The data variables listed under Metadata are included for both radiance and irradiance calculations. N<sub>x</sub>,  
 1274 N<sub>y</sub>, and N<sub>z</sub> are the number of pixels along x, y, and z direction, respectively. N<sub>g</sub> is the number of g,  
 1275 explained in [Appendix A2 – Correlated-k](#).

Deleted: 1

1276

1277 **A2 – EaR<sup>3</sup>T Code Walk-through**

1278 We will provide a code walk-through of the OCO-2 and MODIS simulator applications  
 1279 with the codes [examples/01\\_oco2\\_rad-sim.py](#) (App. 1) and  
 1280 [examples/02\\_modis\\_rad-sim.py](#) (App. 2). The data acquisition (first step in Figure 1)

Deleted: section 3

1283 uses functions in `er3t/util`. App. 1 and App. 2 use the functions in `er3t/util/modis.py`  
1284 and `er3t/util/oco2.py` for downloading the MODIS and OCO-2 data files from the  
1285 respective NASA data archives and for processing the data (e.g., geo-mapping, gridding etc.). The  
1286 user supplies minimum input (date and time, as well as latitudes and longitudes of the region of  
1287 interest), which need to be specified in `satellite_download` (within the application codes).  
1288 For example, for App. 1 and App. 2, the only user inputs are the date and time and the region of  
1289 interest – in this case September 2, 2019, with the westernmost, easternmost, southernmost, and  
1290 northernmost longitudes and latitudes of 109°W, 107°W, 37°N, and 39°N. In order for EaR<sup>3</sup>T to  
1291 access any data archives such as NASA Earthdata, the user needs to create an account with them  
1292 and store the credentials locally (detailed instructions are provided separately along with the EaR<sup>3</sup>T  
1293 distribution).

1294 After the data acquisition step, the satellite data are fed into the pre-processing step for 1)  
1295 atmospheric gases (`er3t/pre/atm`), 2) clouds (`er3t/pre/cld`), 3) surface  
1296 (`er3t/pre/sfc`) as shown in Figure 1. In the default configuration of the App. 1, the standard  
1297 US atmosphere (Anderson et al., 1986; included in the EaR<sup>3</sup>T repository) is used within `atm`.  
1298 EaR<sup>3</sup>T supports the input of user-specified atmospheric profiles, e.g., atmospheric profiles from  
1299 reanalysis data for App. 2 as described in Chen et al. (2023), by making changes in `atm_atmmod`  
1300 (from `er3t/pre/atm`). Subsequently, molecular scattering coefficients are calculated by  
1301 `cal_mol_ext` (from `er3t/util`), and absorption coefficients for atmospheric gases are  
1302 generated by (`er3t/pre/abs`). At the current development stage, two options are available:

1303 1. Line-by-line (used by App. 1): The repository includes a sample file of absorption coefficient  
1304 profiles for a subset of wavelengths within OCO-2's Oxygen A-Band channel, corresponding  
1305 to a range of atmospheric transmittance values from low (opaque) to high (so-  
1306 called "continuum" wavelength). They were generated by an external code (Chen et al., 2023)  
1307 based on OCO-2's line-by-line absorption coefficient database (ABSCO, Payne et al., 2020).  
1308 They are calculated for a fixed mixing ratio of 400 ppm. In a subsequent paper (Chen et al.,  
1309 2023), an OCO-2 specific EaR<sup>3</sup>T code will be published where the actual mixing ratio is  
1310 used. For each OCO-2 spectrometer wavelength within a given channel, hundreds of  
1311 individual absorption coefficient profiles at the native resolution of ABSCO need to be  
1312 considered across the instrument line shape (ILS, also known as the slit function) of the  
1313 spectrometer. The ILS, as well as the incident solar irradiance, are also included in the file.

1314 In subsequent steps, EaR<sup>3</sup>T performs RT calculations at the native spectral resolution of  
1315 ABSCO, but then combines the output by convolving with the ILS and outputs OCO-2  
1316 radiances or reflectances at the subset of wavelengths. For probabilistic (Monte Carlo) RT  
1317 solvers such as MCARaTS, the number of photons can be kept relatively low (e.g., 10<sup>6</sup>  
1318 photons), and can be adjusted according to the values of the ILS at a particular ABSCO  
1319 wavelength. Any uncertainty at the ABSCO spectral resolution due to photon noise is greatly  
1320 reduced by convolving with the ILS for the final output.

1321 2. Correlated-k (used by App. 2): This approach (Mlawer et al., 1997) is appropriate for  
1322 instruments such as MODIS with much coarser spectral resolution than OCO-2, as well as  
1323 for broadband calculations. In contrast to the line-by-line approach, RT calculations are not  
1324 performed at the native resolution of the absorption database, but at Gaussian quadrature  
1325 points (called “g’s”) that represent the full range of sorted absorption coefficients, and then  
1326 combined using Gaussian quadrature weights. The repository includes an absorption  
1327 database from Coddington et al. (2008), developed specifically for a radiometer with  
1328 moderate spectral resolution on the basis of HITRAN (high-resolution transmission  
1329 molecular absorption database) 2004 (Rothman et al., 2005). It was created for the ILS of  
1330 the airborne Solar Spectral Flux Radiometer (SSFR, Pilewskie et al., 2003), but is applied to  
1331 MODIS here, which has a moderate spectral resolution of 8-12 nm with 20-50 nm  
1332 bandwidths. It uses 16 absorption coefficient bins (g’s) per target wavelength (this could  
1333 either be an individual SSFR or a MODIS channel), which are calculated by EaR<sup>3</sup>T with the  
1334 Coddington et al. (2008) database using the mixing ratios of atmospheric gases in the  
1335 previously ingested profile. In future implementations, the code will be updated to enable  
1336 flexible ILS and broadband calculations.

1337 The er3t/pre/cld module calculates extinction, thermodynamic phase, and effective  
1338 droplet radius of clouds from the input data. The er3t/pre/pha module creates the required  
1339 single scattering albedo and scattering phase function. The default is a Henyey-Greenstein phase  
1340 function with a fixed asymmetry parameter of 0.85. Along with the current distribution (v0.1.1) of  
1341 EaR<sup>3</sup>T, the Mie phase functions based on thermodynamic phase, effective droplet radius, and  
1342 wavelength are supported. In this study, App. 1 and App. 2 use Mie phase functions calculated  
1343 from Legendre polynomial coefficients (originally distributed along with libRadtran) based on the  
1344 wavelength and cloud droplet effective radius. In the future, EaR<sup>3</sup>T will include stand-alone phase

1345 functions, which can be chosen on the basis of droplet size distributions in addition to effective  
1346 radius. It is also possible to include aerosols in a similar fashion as clouds. This is done with the  
1347 er3t/pre/aer module. In the case of aerosols, spectral single scattering albedo and asymmetry  
1348 parameter are required as inputs in addition to the extinction fields.

1349 After the optical properties are calculated, they are passed into the 3D-RT step  
1350 (er3t/rtm/mca). This step performs the setup of RT solver-specified input parameters and data  
1351 files, distributing runs over multiple Central Processing Units (CPUs), and post-processing RT  
1352 output files into a single, user-friendly HDF5 file. For example, when radiance is specified as  
1353 output (default in App. 1 and App. 2), key information such as the radiance field and its standard  
1354 deviation are stored in the final HDF5 file (details see Table 1).

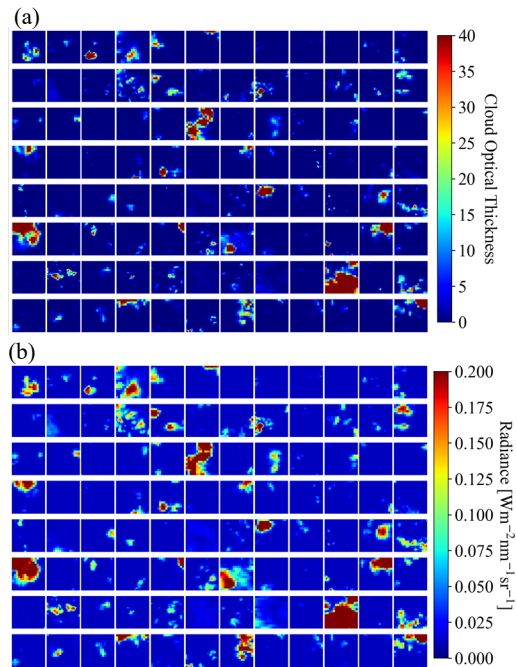
1355 While the EaR<sup>3</sup>T repository comes with various applications such as App. 1 and App. 2,  
1356 described above, the functions used by these master or ‘wrapper’ programs can be organized in  
1357 different ways, where the existing applications serve as templates for a quick start when developing  
1358 new applications. The functions used by the master code pass information through the various  
1359 steps as Python objects. For example, in examples/01\_oco2\_rad-sim.py, the downloaded  
1360 and processed satellite data are stored into the sat object. Later, the sat object is passed into an  
1361 EaR<sup>3</sup>T function to create the cld object that contains cloud optical properties. Similarly, EaR<sup>3</sup>T  
1362 provides functions to create the atm, and sfc objects with optical properties for atmospheric  
1363 gases and the surface. These objects (atm, cld, sfc) are in turn passed on to solver-specific  
1364 modules for performing RT calculations. The user can choose to save the data of the intermediate  
1365 objects into Python pickle files after the first run. In this way, multiple calls with identical input  
1366 can re-use existing data, which accelerates the processing time of EaR<sup>3</sup>T. Unless the user specifies  
1367 the overwrite keyword argument in the object call to reject saving pickle files, these shortcuts  
1368 save significant time.

1369

## 1370 **Appendix B – App. 5 Radiance calculations based on the Large Eddy Simulation**

1371 The CNN COT retrieval framework was developed by Nataraja et al. (2022). It adapts a  
1372 U-Net (Ronneberger et al., 2015) architecture and treats the retrieval of COT from radiance as a  
1373 segmentation problem – probabilities of 36 COT classes (ranging from COT of 0 to 100) are  
1374 returned as the final COT retrieved for a given cloud radiance field. It accounts for horizontal  
1375 photon transport, which is neglected in traditional cloud retrieval algorithms; in other words, for

1376 the spatial context of cloudy pixels. It was trained on synthetic cloud fields generated by a Large  
1377 Eddy Simulation (LES) model, which provides the ground truth of COT. Subsequently, EaR<sup>3</sup>T was  
1378 used to calculate 3D-RT radiances at 600 nm for LES cloud fields to establish a mapping between  
1379 radiance to COT. Only six LES cases were used to represent the variability of the cloud  
1380 morphology. Each of these fields are 480x480 pixels across (spatial resolution of 100 m). These  
1381 large fields were mapped onto thousands of 64x64 mini tiles with spatial resolution of 100 m as  
1382 described in Nataraja et al., 2022. To keep the training data set small, mini tiles selectively sampled  
1383 according to their mean COT and standard deviation. This ensured an even representation of the  
1384 dynamic range of COT and its variability, which was termed homogenization of the training data  
1385 set. Figure A1 shows a collection of samples from the training data as an illustration. All the  
1386 aforementioned simulation setup and techniques in data process are included in the App. 5 example  
1387 code, which can be applied to the LES data (a different scene from the 6 scenes) distributed along  
1388 with EaR<sup>3</sup>T.  
1389



1390

1391

1392 **Figure A1.** Illustrations of 64x64 tiles of (a) cloud optical thickness from LES data and (b) calculated 3D radiance at  
 1393 600 nm from EaR<sup>3</sup>T for CNN training.

1394  
 1395 **Appendix C**

1396 **C1. Cloud Detection/Identification**

1397 Cloudy pixels are identified through a thresholding method based on the red, green, and  
 1398 blue channels of MODIS. When the radiance values of the red, green, and blue channels of a pixel  
 1399 are all greater than a pre-calculated threshold value, the pixel is considered as cloudy, as illustrated  
 1400 by the following equation

$$1401 \text{ If } \begin{cases} \text{Red} > a_R \cdot \text{Quantile}(\text{Red}, q_0) \ \& \\ \text{Blue} > a_B \cdot \text{Quantile}(\text{Blue}, q_0) \ \& \\ \text{Green} > a_G \cdot \text{Quantile}(\text{Green}, q_0) \end{cases} \begin{cases} \text{Yes: cloudy} \\ \text{No: clear sky} \end{cases} \quad (A1)$$

1402 where  $a_R, a_B,$  and  $a_G$  are scale factors with a default value of 1.0, and  $\text{Quantile}$  returns the  $q_0$   
 1403 percentile of the sorted reflectance data (ascending order;  $q_0 = 0.5$  is equivalent to the median).  
 1404 The scale factors can be adjusted separately to perform fine tuning for different surface types. For  
 1405 example, adjusting  $a_G$  will be more effective for separating clouds from greenish vegetation  
 1406 surface than the other two factors. For simplicity, they are all set to 1.0 for the case shown in App.  
 1407 1 and 2. The  $q_0$  is determined by the following equation,

$$1408 q_0 = \max(0, 1 - \text{frac}_{\text{cld}} \cdot 1.2) \quad (A2)$$

1409 where  $\text{frac}_{\text{cld}}$  is cloud fraction obtained from the MODIS L2 cloud product (number of cloudy  
 1410 pixels divided by the number of total pixels). Through the definition of  $q_0$ , the threshold-based  
 1411 cloud detection method is pegged to the MODIS product at the domain scale. Because of the coarse  
 1412 resolution of the MODIS-based cloud mask, it cannot be used directly for our application.  
 1413 However, it uses many more channels than available at high spatial resolution, and is therefore  
 1414 more accurate. The factor of 1.2 can be adjusted. A value of higher than 1 allows for clouds that  
 1415 are not detected by MODIS (for various reasons, for example because of their spatial scale) to be  
 1416 picked up. At the same time, this leads to over-detection (false positives, i.e. clear-sky pixels  
 1417 identified as cloudy), and therefore the thresholding is only the first step (primary thresholding),  
 1418 followed by the next (secondary) step where false positives are removed.

1419 The secondary step is based on MODIS L2 cloud products:  $COT$  (cloud optical thickness),  
 1420  $CER$  (cloud effective radius), and  $CTH$  (cloud top height). For the pixels that are identified as  
 1421 cloudy in the primary thresholding, especially at the lower end of the reflectance ( $Ref.$ ), we rely

Deleted: simple

Deleted: the corresponding median value

Deleted: Median

Deleted: Median

Deleted: Median

Deleted: ,

Deleted: ,

Deleted:

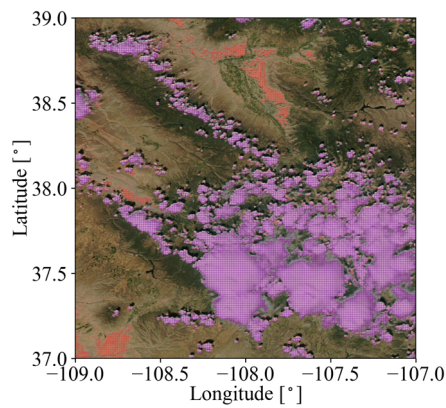


1430 on the clear-sky identifiers from MODIS L2 cloud product (where no cloud products are retrieved),  
1431 as illustrated by the following equation

1432 
$$\text{If } \begin{cases} \text{Ref.} < \text{Median}(\text{Ref.}) \ \& \\ \text{COT, CER, and CTH are NaN} \end{cases} \begin{cases} \text{Yes: clear sky} \\ \text{No: cloudy} \end{cases} \quad (\text{A3})$$

1433 Figure A2 shows the cloud mask from primary thresholding (Equation A1, red and purple), and  
1434 the pixels that are reverted to clear-sky by the secondary filter (Equation A2, red),

1435



1436

1437 **Figure A2.** Cloud mask for the scene shown in Figure 2. Red and purple indicate pixels identified as cloudy through  
1438 the primary thresholding (Equation A1) and purple indicates pixels finally identified as cloudy after applying  
1439 secondary filter (Equation A3).

1440

## 1441 C2. IPA Reflectance-to-COT Mapping

1442 In order to retrieve COT (cloud optical thickness) from cloud reflectance as measured by  
1443 various instruments, we use the EaR<sup>3</sup>T built-in solver MCARaTS in IPA mode to calculate a  
1444 lookup table of reflectance as a function of COT. The function for generating these lookup tables  
1445 is included in EaR<sup>3</sup>T as `er3t.rtm.mca.func_ref_vs_cot`. Two mappings are generated  
1446 for App. 1&2 to account for geometrically thin (cloud top height less than 4 km) and thick (cloud  
1447 top height greater than 4 km) clouds separately while a single mapping is generated for App. 4.  
1448 Specifically, for a range of COT (0 to 200), reflectance is calculated from EaR<sup>3</sup>T with the same  
1449 input parameters (wavelength, viewing and solar geometries, and surface albedo) listed in Table  
1450 A1 for each application except for a few simplifications described in the following table (Table  
1451 A3):

**Deleted:** Note that this only works for partially cloud-covered scenes, and may lead to false positives if there is brightness contrast from objects other than clouds. This method was specifically applied for the cases in this paper and should be changed as appropriate for future applications.

**Deleted:** Two-Stream Approximation

1458

| Cloud Type                     | App. 1 & 2                                |   | App. 4           |
|--------------------------------|---|---|------------------|
|                                | Geometrically Thin<br>Clouds              | Geometrically Thick<br>Clouds             | All              |
| Cloud Effective Radius         | 10 $\mu\text{m}$                          | 20 $\mu\text{m}$                          | 10 $\mu\text{m}$ |
| Cloud Top Height               | 3 km                                      | 10 km                                     | 2 km             |
| Cloud Geometrical<br>Thickness | 1 km                                      | 7 km                                      | 1 km             |
| Surface Albedo                 | 0.08 (domain average of<br>the MCD43 WSA) | 0.08 (domain average of<br>the MCD43 WSA) | 0.03             |

1459

1460 **Table A3:** List of parameters for deriving IPA reflectance-to-COT (cloud optical thickness) mappings for App. 1&2  
 1461 and App. 4 in addition to Table A1.

1462

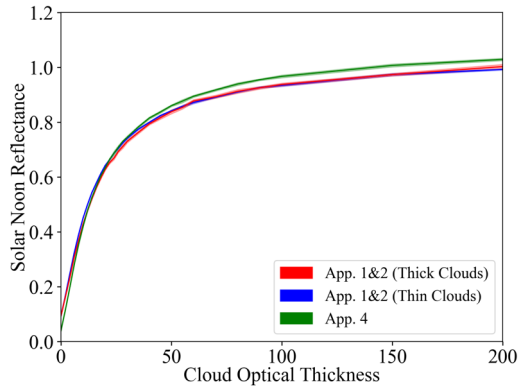
1463 The clouds are assumed horizontally homogeneous over a  $2 \times 2$  pixel domain. For each  
 1464 calculation,  $10^8$  photons are used for running EaR<sup>3</sup>T in IPA mode. After calculating  $R(COT)$ , the  
 1465 inverse relationship of  $COT(R)$  is then used for estimating  $COT$  at any given  $R$  for the cloudy  
 1466 pixels. Figure A3 shows the IPA reflectance-to-COT mappings created for App. 1&2, and App 4.  
 1467 Note that the difference between the App. 1&2 thin clouds (blue) and App. 4 (green) is due to  
 1468 different surface albedos (when COT less than 20) and sensor viewing geometries (when COT  
 1469 greater than 20, specified in Table A1). Note that this approach will ensure IPA  
 1470 radiance/reflectance consistency (retrieved IPA COT will reproduce the exact IPA cloud  
 1471 reflectance, see Figure A4) because the radiative transfer processes of  $R(COT)$  and  $COT(R)$  are  
 1472 the same. However, since it makes some simplifications as mentioned above, uncertainties are  
 1473 expected for a complicated atmospheric environment (varying cloud thermodynamic phase,  
 1474 effective radius, cloud top height, geometrical thickness, vertical profile; variable surface albedo  
 1475 and topography), which are shown up as spread (deviations from identity line) in Figure A4.  
 1476

**Deleted:** The two-stream approximation of the reflectance  $R$  is calculated using Eq. D2 from Chen et al. (2021), as follows:

**Deleted:**  $\tau$

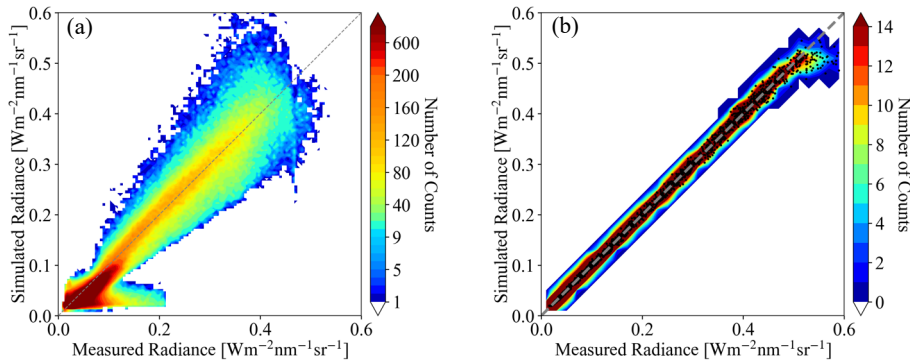
**Deleted:**  $\tau$

**Deleted:** does not take into account any cloud reflectance anisotropies.



1484  
1485  
1486  
1487  
1488

**Figure A3.** The IPA reflectance-to-COT mappings used for App. 1&2 (red and blue) and App. 4 (green). The reflectance is normalized by the cosine of solar zenith angle (referred to as solar noon reflectance). The uncertainties associated with photon statistics are indicated by the shaded area.



1489  
1490  
1491  
1492

**Figure A4.** (a) and (b) are the same as Figure 7 and Figure 13b except for the IPA radiance calculations.

## 1493 Appendix D

### 1494 D1. Parallax Correction

1495 From the satellite's view, the clouds (especially high clouds) will be placed at inaccurate  
1496 locations on the surface, which have shifted from their actual locations due to the parallax effect.

1497 We followed simple trigonometry to correct for it, as follows:

Deleted: simply

1499 Longitude correction (positive from west to east):

$$1500 \quad \delta lon = \frac{(z_{cld} - z_{sfc}) \cdot \tan(\theta) \cdot \sin(\phi)}{\pi \cdot R_{Earth}} \times 180^\circ \quad (A4)$$

1501 Latitude correction (positive from south to north):

$$1502 \quad \delta lat = \frac{(z_{cld} - z_{sfc}) \cdot \tan(\theta) \cdot \cos(\phi)}{\pi \cdot R_{Earth}} \times 180^\circ \quad (A5)$$

1503 where  $(lon_{sat}, lat_{sat}, z_{sat})$  is the satellite location and  $\theta$  and  $\phi$  ( $0^\circ$  at north, positive clockwise)  
1504 are the sensor viewing zenith and azimuth angles.  $z_{cld}$  and  $z_{sfc}$  are the cloud top height and the  
1505 surface height.  $R_{Earth}$  is the radius of the Earth. Figure A2 shows an illustration of the parallax  
1506 correction for the cloud field in the inset in Figure 2. Note that discontinuities in the latitude and  
1507 longitude fields arising from different combinations of sensor viewing geometries and cloud top  
1508 and surface heights may lead to gaps in the cloud fields. These gaps are identified and filled in  
1509 with the average of data from adjacent pixels (plus minus two pixels along x and y) through the  
1510 following process:

1511 **If**  $pixel_{ij}^{aft}$  is clear &  $pixel_{ij}^{bef}$  is cloudy &  $\left\{ \begin{array}{l} cldfrac(pixel^{bef}[i-2:i+2, j-2:j+2]) > frac_a \& \\ cldfrac(pixel^{aft}[i-2:i+2, j-2:j+2]) > frac_b \& \end{array} \right. \left\{ \begin{array}{l} \text{Yes: fill } pixel_{ij}^{aft} \text{ with the average of} \\ \end{array} \right.$

1512 where  $pixel_{ij}$  indicates the pixel at  $i$  along x and  $j$  along y,  $bef$  and  $aft$  refer to before and after  
1513 parallax correction respectively,  $cldfrac$  calculates cloud fraction (number of cloudy pixels  
1514 divided by total pixel number), and  $cld$  selects data where pixels are identified as cloudy. The  
1515  $frac_a$  and  $frac_b$  are set to 0.7 for the cases demonstrated in the paper. Lower  $frac_a$  tends to over  
1516 select clear-sky pixels at the cloud edge and lower  $frac_b$  tends to over correct clear-sky pixels  
1517 within clouds that are not clear-sky due to parallax artifacts. While increase  $frac_a$  and  $frac_b$   
1518 tends to under correct parallax artifacts.

1519

## 1520 D2. Wind Correction

1521 The wind correction aims at correcting the movement of clouds when advected by the wind  
1522 between two different satellites' overpasses.

1523 Longitude correction (positive from west to east):

$$1524 \quad \delta lon = \frac{u \cdot \delta t}{\pi \cdot R_{Earth}} \times 180^\circ \quad (A6)$$

Deleted: B1

Deleted: B2

Deleted: B3

1528 Latitude correction (positive from south to north):

1529 
$$\delta lat = \frac{v \cdot \delta t}{\pi \cdot R_{Earth}} \times 180^\circ$$

(A7)

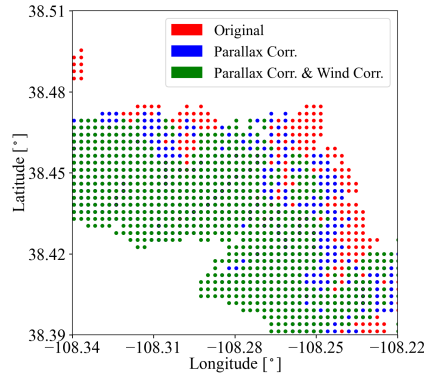
Deleted: B4

1530 where  $u$  and  $v$  are the domain-averaged 10 m zonal and meridional wind speeds, and  $\delta t$  is the time  
1531 difference between two different satellites that fly on the same orbit. Figure A2 shows the cloud  
1532 location after applying the parallax (Appendix D1) and wind correction for the cloud field in the  
1533 inset from Figure 2.

1534

1535

1536



1537

1538 **Figure A5.** An illustration of correcting cloud location (red) for parallax effect (blue) and wind effect (green) for the  
1539 cloud field of the inset in Figure 2. Filled cloud gaps as described in Appendix D1 are indicated by black  
1540 circles.

Deleted: A2

1541

1544 **Acknowledgement**

1545 The aircraft all-sky camera was radiometrically calibrated by the U.S. Naval Research Laboratory.

1546 We thank Jens Redemann for insightful discussions [on Figure 9 \(App. 3\)](#) about the apparent  
1547 contradiction of the direction of the COT, reflectance, and transmittance biases.

Deleted: about

1548

1549 **Data availability**

1550 For App. 1 and App. 2, the OCO-2 data were provided by the NASA Goddard Earth Sciences Data  
1551 and Information Services Center (GES DISC, <https://oco2.gesdisc.eosdis.nasa.gov/data>) and the  
1552 MODIS data were provided by the NASA Goddard Space Flight Center's Level-1 and Atmosphere  
1553 Archive and Distribution System (LAADS, <https://ladsweb.modaps.eosdis.nasa.gov/archive>),  
1554 which are all publicly available and can be downloaded by EaR<sup>3</sup>T through the application code.

1555 For App. 3, the AHI data were processed by Holz's (coauthor of this paper) team. The SPN-S data  
1556 were provided by Schmidt and Norgren (coauthors of this paper). Both the AHI and SPN-S data  
1557 are publicly available at NASA Airborne Science Data for Atmospheric Composition  
1558 (<https://www-air.larc.nasa.gov/missions/camp2ex/index.html>). The AHI data and the SPN-S data  
1559 for the flight track indicated in Figure 8 of the paper are distributed along with EaR<sup>3</sup>T for  
1560 demonstration purpose. For App. 4, all sky camera imagery and CNN model are distributed along  
1561 with EaR<sup>3</sup>T. EaR<sup>3</sup>T is publicly available and can be accessed and downloaded at  
1562 <https://github.com/hong-chen/er3t> (or <https://doi.org/10.5281/zenodo.7734965> for v0.1.1, used in  
1563 this paper; Chen and Schmidt, 2022).

Deleted: 10.5281/zenodo.7374196

Deleted: 0.1.0

1564

1565 **Author contributions**

1566 All the authors helped with editing the paper. HC developed the EaR<sup>3</sup>T package in Python  
1567 including the application code, performed the analysis, and wrote the majority of the paper with  
1568 input from the other authors. KSS provided [an initial](#) MCARaTS simulation wrapper code in  
1569 Interactive Data Language (IDL); helped with the structure design of EaR<sup>3</sup>T; and helped with  
1570 interpreting the results and writing the paper. SM helped with the OCO-2 data interpretation. VN  
1571 trained and provided the CNN model. MN helped with the SPN-S instrument calibration and data  
1572 processing. JG and GF helped with testing EaR<sup>3</sup>T and the LES data interpretation. RH provided  
1573 the AHI data and helped with the data interpretation. HI helped with the implementation of  
1574 MCARaTS [in](#) EaR<sup>3</sup>T.

Deleted: into

1579 **References**

- 1580 Anderson, G. P., Clough, S. A., Kneizys, F. X., Chetwynd, J. H., and Shettle, E. P.: AFGL  
1581 atmospheric constituent profiles (0–120 km), Tech. Rep. AFGL-TR-86-0110, Air Force  
1582 Geophys. Lab., Hanscom Air Force Base, Bedford, Massachusetts, U.S.A., 1986.
- 1583 Barker, H. and Liu, D.: Inferring optical depth of broken clouds from Landsat data, *J. Climate*, 8,  
1584 2620–2630, 1995.
- 1585 Barker, H. W., Jerg, M. P., Wehr, T., Kato, S., Donovan, D. P., and Hogan, R. J.: A 3D cloud  
1586 construction algorithm for the EarthCARE satellite mission, *Q. J. Roy. Meteor. Soc.*, 137,  
1587 1042–1058, <https://doi.org/10.1002/qj.824>, 2011.
- 1588 Barker, H. W., Kato, S., and Wehr, T.: Computation of solar radiative fluxes by 1-D and 3-D  
1589 methods using cloudy atmospheres inferred from A-train satellite data, *Surv. Geophys.*, 33,  
1590 657–676, 2012.
- 1591 Cahalan, R., Oreopoulos, L., Marshak, A., Evans, F., Davis, A., Pincus, R., Yetzen, K. H., Mayer,  
1592 B., Yetzer, K. H., Mayer, B., Davies, R., Ackerman, T. P., Barker, H. W., Clothiaux, E. E.,  
1593 Ellingson, R. G., Garay, M. J., Kassianov, E., Kinne, S., Macke, A., O'Hirok, W., Partain, P.  
1594 T., Prigarin, S. M., Rublev, A. N., Stephens, G. L., Szczap, F., Takara, E. E., Varnai, T., Wen,  
1595 G., and Zhuravleva, T.: The I3RC: Bringing Together the Most Advanced Radiative Transfer  
1596 Tools for Cloudy Atmospheres, *B. Am. Meteorol. Soc.*, 86, 1275–1293, 2005.
- 1597 Chen, H. and Schmidt, S.: er3t-~~v0.1.1~~, <https://doi.org/10.5281/zenodo.7734965>, 2023.
- 1598 Chen, H., Schmidt, S., and Holz, R. E.: Synchronized Flight Videos for NASA CAMP<sup>2</sup>Ex,  
1599 <https://doi.org/10.5281/zenodo.7358509>, 2022.
- 1600 [Chen, Y.-W., Schmidt, S., Massie, S., Chen, H., Crisp, D., Kulawik, S., Merrelli, A., McDuffie, J.,  
1601 Iwabuchi, H.: Uncovering the Mechanism for Trace Gas Spectroscopy Biases in the Vicinity  
1602 of Clouds With the OCO-2 3D Radiative Transfer Satellite Radiance Simulator, \*Atmos. Meas.  
1603 Tech., in prep., 2023.\*](#)
- 1604 Crisp, D.: Measuring Atmospheric Carbon Dioxide from Space with the Orbiting Carbon  
1605 Observatory-2 (OCO-2), *P. Soc. Photo.-Opt. Ins.*, 9607, 960702,  
1606 <https://doi.org/10.1117/12.2187291>, 2015.
- 1607 Coddington, O., Schmidt, K. S., Pilewskie, P., Gore, W. J., Bergstrom, R., Roman, M., Redemann,  
1608 J., Russell, P. B., Liu, J., and Schaaf, C. C.: Aircraft measurements of spectral surface albedo  
1609 and its consistency with ground-based and space-borne observations, *J. Geophys. Res.*, 113,

Deleted: v0.1.0

Deleted: 10.5281/zenodo.7374196

Deleted: 2022

1613 D17209, doi:10.1029/2008JD010089, 2008.

1614 Deneke, H., Barrientos-Velasco, C., Bley, S., Hünerbein, A., Lenk, S., Macke, A., Meirink, J. F.,  
1615 Schroedter-Homscheidt, M., Senf, F., Wang, P., Werner, F., and Witthuhn, J.: Increasing the  
1616 spatial resolution of cloud property retrievals from Meteosat SEVIRI by use of its high-  
1617 resolution visible channel: implementation and examples, *Atmos. Meas. Tech.*, 14, 5107–  
1618 5126, <https://doi.org/10.5194/amt-14-5107-2021>, 2021.

1619 Deutschmann, T., Beirle, S., Friess, U., Grzegorski, M., Kern, C., Kritten, L., Platt, U., Prados-  
1620 Roman, C., Pukite, J., Wagner, T., Werner, B., and Pfeilsticker, K.: The Monte Carlo  
1621 atmospheric radiative transfer model McArtim: introduction and validation of Jacobians and  
1622 3-D features, *J. Quant. Spectrosc. Ra.*, 112(6), 1119–1137, ISSN 0022-4073,  
1623 doi:10.1016/j.jqsrt.2010.12.009, 2011.

1624 Doicu, A., Efremenko, D., and Trautmann, T.: A multi-dimensional vector spherical harmonics  
1625 discrete ordinate method for atmospheric radiative transfer, *J. Quant. Spectrosc. Ra.*, 118,  
1626 121–131, <https://doi.org/10.1016/j.jqsrt.2012.12.009>, 2013.

1627 Emde, C., Barlakas, V., Cornet, C., Evans, F., Korkin, S., Ota, Y., Labonnote, L. C., Lyapustin,  
1628 A., Macke, A., Mayer, B., and Wendisch, M.: IPRT polarized radiative transfer model  
1629 intercomparison project – Phase A, *Journal of Quantitative Spectroscopy and Radiative*  
1630 *Transfer*, 164, 8–36, <https://doi.org/10.1016/j.jqsrt.2015.05.007>, 2015.

1631 Emde, C., Buras-Schnell, R., Kylling, A., Mayer, B., Gasteiger, J., Hamann, U., Kylling, J., Richter,  
1632 B., Pause, C., Dowling, T., and Bugliaro, L.: The libRadtran software package for radiative  
1633 transfer calculations (version 2.0.1), *Geosci. Model Dev.*, 9, 1647–1672,  
1634 <https://doi.org/10.5194/gmd-9-1647-2016>, 2016.

1635 Evans, K. F.: The spherical harmonics discrete ordinate method for three-dimensional atmospheric  
1636 radiative transfer, *J. Atmos. Sci.*, 55, 429–446, 1998.

1637 Gatebe, C. K., Jethva, H., Gautam, R., Poudyal, R., and Várnai, T.: A new measurement approach  
1638 for validating satellite-based above-cloud aerosol optical depth, *Atmos. Meas. Tech.*, 14,  
1639 1405–1423, <https://doi.org/10.5194/amt-14-1405-2021>, 2021.

1640 Gristey, J. J., Feingold, G., Glenn, I. B., Schmidt, K. S., and Chen, H.: Surface Solar Irradiance in  
1641 Continental Shallow Cumulus Fields: Observations and Large-Eddy Simulation, *J. Atmos.*  
1642 *Sci.*, 77, 1065–1080, <https://doi.org/10.1175/JAS-D-19-0261.1>, 2020a.

1643 Gristey, J. J., Feingold, G., Glenn, I. B., Schmidt, K. S., and Chen, H.: On the Relationship



1644 Between Shallow Cumulus Cloud Field Properties and Surface Solar Irradiance, *Geophysical*  
1645 *Research Letters*, 47, e2020GL090152, <https://doi.org/10.1029/2020GL090152>, 2020b.

1646 Gristey, J. J., Feingold, G., Glenn, I. B., Schmidt, K. S., and Chen, H.:  
1647 Influence of Aerosol Embedded in Shallow Cumulus Cloud Fields on the Surface Solar  
1648 Irradiance, *Journal of Geophysical Research: Atmospheres*, 127, e2022JD036822,  
1649 <https://doi.org/10.1029/2022JD036822>, 2022.

1650 Heidinger, A. K., Foster, M. J., Walther, A., and Zhao, X.: The Pathfinder Atmospheres-Extended  
1651 AVHRR climate dataset, *B. Am. Meteorol. Soc.*, 95, 909–922,  
1652 <https://doi.org/10.1175/BAMS-D-12-00246.1>, 2014.

1653 Illingworth, A. J., Barker, H. W., Beljaars, A., Chepfer, H., Delanoe, J., Domenech, C., Donovan,  
1654 D. P., Fukuda, S., Hiraoka, M., Hogan, R. J., Huenerbein, A., Kollias, P., Kubota, T.,  
1655 Nakajima, T., Nakajima, T. Y., Nishizawa, T., Ohno, Y., Okamoto, H., Oki, R., Sato, K.,  
1656 Satoh, M., Wandinger, U., Wehr, T., and van Zadelhoff, G.: The EarthCARE Satellite: the  
1657 next step forward in global measurements of clouds, aerosols, precipitation and radiation, *B.*  
1658 *Am. Meteorol. Soc.*, 96, 1311–1332, <https://doi.org/10.1175/BAMS-D-12-00227.1>, 2015.

1659 Iwabuchi, H.: Efficient Monte Carlo methods for radiative transfer modeling, *J. Atmos. Sci.*, 63,  
1660 2324–2339, 2006.

1661 Kindel, B. C., Schmidt, K. S., Pilewskie, P., Baum, B. A., Yang, P., and Platnick, S.: Observations  
1662 and modeling of ice cloud shortwave spectral albedo during the Tropical Composition, Cloud  
1663 and Climate Coupling Experiment (TC<sup>4</sup>), *J. Geophys. Res.*, 115, D00J18,  
1664 [doi:10.1029/2009JD013127](https://doi.org/10.1029/2009JD013127), 2010.

1665 King, M., and Platnick, S.: The Earth Observing System (EOS), *Comprehensive Remote Sensing*,  
1666 7, 26, [doi:10.1016/b978-0-12-409548-9.10312-4](https://doi.org/10.1016/b978-0-12-409548-9.10312-4), 2018.

1667 Levis, A., Schechner, Y. Y., Davis, A. B., and Loveridge, J.: Multi-View Polarimetric Scattering  
1668 Cloud Tomography and Retrieval of Droplet Size, *Remote Sens.*, 12, 2831,  
1669 <https://doi.org/10.3390/rs12172831>, 2020.

1670 Li, J., Scinocca, J., Lazare, M., McFarlane, N., von Salzen, K., and Solheim, L.: Ocean Surface  
1671 Albedo and Its Impact on Radiation Balance in Climate Models, *J. Climate*, 19, 6314–6333,  
1672 2006.

1673 Long, C. N., Bucholtz, A., Jonsson, H., Schmid, B., Vogelmann, A., and Wood, J.: A Method of  
1674 Correcting for Tilt from Horizontal in Downwelling Shortwave Irradiance Measurements on

1675 Moving Platforms, *The Open Atmospheric Science Journal*, 4, 78–87, 2010.

1676 Lloveridge, J., Levis, A., Di Girolamo, L., Holodovsky, V., Forster, L., Davis, A. B., and Schechner,  
1677 Y. Y.: Retrieving 3D distributions of atmospheric particles using Atmospheric Tomography  
1678 with 3D Radiative Transfer – Part 1: Model description and Jacobian calculation, *Atmos.*  
1679 *Meas. Tech. Discuss.* [preprint], <https://doi.org/10.5194/amt-2022-251>, in review, 2022.

1680 Masuda, R., Iwabuchi, H., Schmidt, K. S., Damiani, A. and Kudo, R.: Retrieval of Cloud Optical  
1681 Thickness from Sky-View Camera Images using a Deep Convolutional Neural Network  
1682 based on Three-Dimensional Radiative Transfer, *Remote Sensing*, 11(17), 1962,  
1683 doi:10.3390/rs11171962, 2019.

1684 Marshak, A., Davis, A., Wiscombe, W., and Cahalan, R.: Radiative smoothing in fractal clouds, *J.*  
1685 *Geophys. Res.*, 100, 26247–26261, <https://doi.org/10.1029/95JD02895>, 1995.

1686 Marshak, A., Wen, G., Coakley, J., Remer, L., Loeb, N. G., and Cahalan, R. F.: A simple model  
1687 for the cloud adjacency effect and the apparent bluing of aerosols near clouds, *J. Geophys.*  
1688 *Res.*, 113, D14S17, <https://doi.org/10.1029/2007JD009196>, 2008.

1689 Massie, S. T., Schmidt, K. S., Eldering, A., and Crisp, D.: Observational evidence of 3-D cloud  
1690 effects in OCO-2 CO<sub>2</sub> retrievals, *J. Geophys. Res. Atmos.*, 122, 7064–7085,  
1691 <https://doi.org/10.1002/2016JD026111>, 2017.

1692 Mayer, B. and Kylling, A.: Technical note: The libRadtran software package for radiative transfer  
1693 calculations – description and examples of use, *Atmos. Chem. Phys.*, 5, 1855–1877,  
1694 <https://doi.org/10.5194/acp-5-1855-2005>, 2005.

1695 Mayer, B.: Radiative transfer in the cloudy atmosphere, *EPJ Web of Conferences*, 1, 75–99,  
1696 doi:10.1140/epjconf/e2009-00912-1, 2009.

1697 Mlawer, E. J., Taubman, S. J., Brown, P. D., Iacono, M. J., and Clough, S. A.: Radiative transfer  
1698 for inhomogeneous atmospheres: RRTM, a validated correlated-k model for the longwave, *J.*  
1699 *Geophys. Res.*, 102, 16663–16682, 1997.

1700 Nakajima, T. and King, M. D.: Determination of the optical thickness and effective particle radius  
1701 of clouds from reflected solar radiation measurements. Part I: Theory, *J. Atmos. Sci.*, 47,  
1702 1878–1893, 1990.

1703 Nataraja, V., Schmidt, S., Chen, H., Yamaguchi, T., Kazil, J., Feingold, G., Wolf, K., and Iwabuchi,  
1704 H.: Segmentation-Based Multi-Pixel Cloud Optical Thickness Retrieval Using a  
1705 Convolutional Neural Network, *Atmos. Meas. Tech.*, 15, 5181–5205, doi:10.5194/amt-15-

1706 5181-2022, 2022.

1707 Norgren, M. S., Wood, J., Schmidt, K. S., van Diedenhoven, B., Stammes, S. A., Ziemba, L. D.,  
1708 Crosbie, E. C., Shook, M. A., Kittelman, A. S., LeBlanc, S. E., Broccardo, S., Freitag, S., and  
1709 Reid, J. S.: Above-aircraft cirrus cloud and aerosol optical depth from hyperspectral  
1710 irradiances measured by a total-diffuse radiometer, *Atmos. Meas. Tech.*, 15, 1373–1394,  
1711 <https://doi.org/10.5194/amt-15-1373-2022>, 2022.

1712 Payne, V. H., Drouin, B. J., Oyafuso, F., Kuai, L., Fisher, B. M., Sung, K., Nemchicka, D.,  
1713 Crawford, T. J., Smyth, M., Crisp, D., Adkins, E., Hodges, J. T., Long, D. A., Mlawer, E. J.,  
1714 Merrelli, A., Lunny, E., and O’Dell, C. W.: Absorption coefficient (ABSCO) tables for the  
1715 Orbiting Carbon Observatories: version 5.1, *J. Quant. Spectrosc. Ra.*, 255, 1–16,  
1716 <https://doi.org/10.1016/j.jqsrt.2020.107217>, 2020.

1717 Pilewskie, P., Pommier, J., Bergstrom, R., Gore, W., Howard, S., Rabbette, M., Schmid, B., Hobbs,  
1718 P. V., and Tsay, S. C.: Solar spectral radiative forcing during the Southern African Regional  
1719 Science Initiative, *J. Geophys. Res.*, 108, 8486, <https://doi.org/10.1029/2002JD002411>, 2003.

1720 Pincus, R. and Evans, K. F.: Computational cost and accuracy in calculating three-dimensional  
1721 radiative transfer: Results for new implementations of Monte Carlo and SHDOM, *J. Atmos.*  
1722 *Sci.*, 66, 3131–3146, 2009.

1723 Platnick, S., King, M. D., Ackerman, S. A., Menzel, W. P., Baum, B. A., Riédi, J. C., and Frey, R.  
1724 A.: The MODIS cloud products: Algorithms and examples from Terra, *IEEE T. Geosci.*  
1725 *Remote*, 41, 459–473, 2003.

1726 [Reid, J. S., Maring, H. B., Narisma, G. T., van den Heever, S., Di Girolamo, L., Ferrare, R.,](#)  
1727 [Lawson, P., Mace, G. G., Simpas, J. B., Tanelli, S., Ziemba, L., van Diedenhoven, B.,](#)  
1728 [Bruitjes, R., Bucholtz, A., Cairns, B., Cambaliza, M. O., Chen, G., Diskin, G. S., Flynn, J.](#)  
1729 [H., Hostetler, C. A., Holz, R. E., Lang, T. J., Schmidt, K. S., Smith, G., Sorooshian, A.,](#)  
1730 [Thompson, E. J., Thornhill, K. L., Trepte, C., Wang, J., Woods, S., Yoon, S., Alexandrov,](#)  
1731 [M., Alvarez, S., Amiot, C. G., Bennett, J. R., Brooks, M., Burton, S. P., Cayanan, E., Chen,](#)  
1732 [H., Collow, A., Crosbie, E., DaSilva, A., DiGangi, J. P., Flagg, D. D., Freeman, S. W., Fu,](#)  
1733 [D., Fukada, E., Hilario, M. R. A., Hong, Y., Hristova-Veleva, S. M., Kuehn, R., Kowch, R.](#)  
1734 [S., Leung, G. R., Loveridge, J., Meyer, K., Miller, R. M., Montes, M. J., Moum, J. N., Nenes,](#)  
1735 [T., Nesbitt, S. W., Norgren, M., Nowotnick, E. P., Rauber, R. M., Reid, E. A., Rutledge, S.,](#)  
1736 [Schlosser, J. S., Sekiyama, T. T., Shook, M. A., Sokolowsky, G. A., Stammes, S. A., Tanaka,](#)

1737 [T. Y., Wasilewski, A., Xian, P., Xiao, Q., Xu, Z., and Zavaleta, J.](#) The coupling between  
1738 tropical meteorology, aerosol lifecycle, convection, and radiation, during the Clouds, Aerosol  
1739 and Monsoon Processes Philippines Experiment (CAMP<sup>2</sup>Ex), *B. Am. Meteorol. Soc.*,  
1740 <https://doi.org/10.1175/BAMS-D-21-0285.1>, 2023.

1741 Ronneberger, O., Fischer, P., and Brox, T.: U-net: Convolutional networks for biomedical image  
1742 segmentation, in: International Conference on Medical image computing and computer-  
1743 assisted intervention, 234–241, Springer, [https://doi.org/10.1007/978-3-319-24574-4\\_28](https://doi.org/10.1007/978-3-319-24574-4_28),  
1744 2015.

1745 Rothman, L., Jacquemart, D., Barbe, A., Chris Benner, D., Birk, M., Brown, L., Carleer, M.,  
1746 Chackerian, C., Chance, K., Coudert, L., Dana, V., Devi, V., Flaud, J.-M., Gamache, R.,  
1747 Gold- man, A., Hartmann, J.-M., Jucks, K., Maki, A., Mandin, J.- Y., Massie, S., Orphal, J.,  
1748 Perrin, A., Rinsland, C., Smith, M., Tennyson, J., Tolchenov, R., Toth, R., Vander Auwera,  
1749 J., Varanasi, P., and Wagner, G.: The HITRAN 2004 molecular spectroscopic database, *J.*  
1750 *Quant. Spectrosc. Ra.*, 96, 139–204, <https://doi.org/10.1016/j.jqsrt.2004.10.008>, 2005.

1751 Schmidt, K. S., Pilewskie, P., Platnick, S., Wind, G., Yang, P., and Wendisch, M.: Comparing  
1752 irradiance fields derived from Moderate Resolution Imaging Spectroradiometer airborne  
1753 simulator cirrus cloud retrievals with solar spectral flux radiometer measurements, *J. Geophys.*  
1754 *Res.*, 112, D24206, doi:10.1029/2007JD008711, 2007.

1755 Schmidt, S., Pilewskie, P., Mayer, B., Wendisch, M., Kindel, B., Platnick, S., King, M. D., Wind,  
1756 G., Arnold, G. T., Tian, L., Heymsfield, G., and Kalesse, H.: Apparent absorption of solar  
1757 spectral irradiance in heterogeneous ice clouds, *J. Geophys. Res.*, 115, D00J22,  
1758 <https://doi.org/10.1029/2009JD013124>, 2010.

1759 [Song, S., Schmidt, K. S., Pilewskie, P., King, M. D., Heidinger, A. K., Walther, A., Iwabuchi, H.,](#)  
1760 [Wind, G., and Coddington, O. M.:](#) The Spectral Signature of Cloud Spatial Structure in  
1761 Shortwave Irradiance, *Atmos. Chem. Phys.*, 16, 13791–13806, [https://doi.org/10.5194/acp-](https://doi.org/10.5194/acp-16-13791-2016)  
1762 [16-13791-2016](https://doi.org/10.5194/acp-16-13791-2016), 2016.

1763 [Strahler, A., Muller, J., Lucht, W., Schaaf, C., Tsang, T., Gao, F., Li, X., Lewis, P., and Barnsley,](#)  
1764 [M.: MODIS BRDF/albedo product: algorithm theoretical basis document version 5.0,](#)  
1765 [MODIS documentation, 1999.](#)

1766 Spada, F., Krol, M. C., and Stammes, P.: McSCIA: application of the Equivalence Theorem in a  
1767 Monte Carlo radiative transfer model for spherical shell atmospheres, *Atmos. Chem. Phys.*,

**Deleted:** Reid, J. S., Maring, H. B., Narisma, G., van den Heever, S., DiGirolamo, L., Ferrare, R., Lawson, P., Mace, G. G., Simpas, J., Tanelli, S., Ziemba, L., van Diedenhoven, B., Bruintjes, R., Bucholtz, A., Cairns, B., Cambaliza, M. O., Chen, G., Diskin, G. S., Flynn, J. H., Hostetler, C. A., Holz, R. E., Lang, T. J., Schmidt, K. S., Smith, G., Sorooshian, A., Thompson, E. J., Thornhill, K. L., Trepte, C., Wang, J., Woods, S., Yoon, S., Alexandrov, M., Alvarez, S., Amiot, C., Bennett, J. R., Brooks, M., Burton, S. P., Cayanan, E., Chen, H., Collow, A., Crosbie, E., DaSilva, A., DiGangi, J. P., Flagg, D. D., Freeman, S. W., Fu, D., Fukada, E., Hilario, M. R. A., Hong, Y., Hristova-Veleva, S. M., Kuehn, R., Kowch, R. S., Leung, G. R., Loveridge, J., Meyer, K., Miller, R., Montes, M. J., Moum, J. N., Nenes, T., Nesbit, S. W., Norgen, M., Novak, E., Rauber, R. M., Reid, E. A., Rutledge, S., Schlosser, J. S., Sekiyama, T. T., Shook, M. A., Sokolowsky, G. A., Stammes, S. A., Sy, O. O., Tanaka, T. Y., Wasilewski, A., Xian, P., Xiao, Q., and Zavaleta, J.

**Deleted:** *in review*,

**Deleted:** 2022

**Moved up [3]:** Chen, Y.-W.,

**Moved (insertion) [3]**

**Deleted:** Chen, Y.-W., Schmidt, S., Massie, S., Chen, H., Crisp, D., Kulawik, S., Chen, Y.-W., Merrelli, A., McDuffie, J., Iwabuchi, H.: Uncovering the Mechanism for Trace Gas Spectroscopy Biases in the Vicinity of Clouds With the OCO-2 3D Radiative Transfer Satellite Radiance Simulator, *Atmos. Meas. Tech.*, *in prep.*, 2022.

1796 6, 4823–4842, <https://doi.org/10.5194/acp-6-4823-2006>, 2006.  
1797 [Várnai, T., A. Marshak, C.-H. Huang: Publicly available online simulator of 3D radiative](#)  
1798 [processes, International Radiation Symposium 2022, Thessaloniki, Greece, 4–8 July 2022,](#)  
1799 [File listed as IRS\\_2022\\_paper\\_89.pdf at](#)  
1800 [General\\_Remote\\_Sensing, 2022.](https://mycloud.auth.gr/index.php/s/t7fYkzsiFWYFdqy?path=/S4-</a><br/>1801 <a href=)  
1802 Wood, J., Smyth, T. J., and Estellés, V.: Autonomous marine hyperspectral radiometers for  
1803 determining solar irradiances and aerosol optical properties, *Atmos. Meas. Tech.*, 10, 1723–  
1804 1737, <https://doi.org/10.5194/amt-10-1723-2017>, 2017.  
1805

**Deleted:** Vermote, E. F., Roger, J. C., and Ray J. P.: MODIS Surface Reflectance User's Guide, MODIS Land Surface Reflectance Science Computing Facility, Version 1.4, 1-35, 2015.

|